Title:

Missing-In-Metastasis / Metastasis Suppressor 1 regulates B cell receptor signaling, B cell metabolic potential and T cell-independent immune responses

Running title: **MIM/MTSS1 regulates B cell activation**

Sarapulov AV[*,†,], Petrov P[*,†], Hernández-Pérez S[*,†,], Šuštar V[*], Kuokkanen E[*], Vainio M[*,†], Cords L[‡], Fritzsche M[‡, §], Carrasco YR[¶], and Mattila PK[*,†]

* *Institute of Biomedicine and MediCity Research Laboratories, University of Turku, Tykistökatu 6B, 20520 Turku, Finland*

† *Turku Bioscience, University of Turku and Åbo Akademi University, 20520 Turku, Finland*

‡ *MRC Human Immunology Unit, Weatherall Institute of Molecular Medicine, University of Oxford, Headley Way, OX3 9DS Oxford, UK*

§ *Kennedy Institute for Rheumatology, Roosevelt Drive, University of Oxford, Oxford OX3 7LF Oxford, UK*

¶ *Department of Immunology and Oncology, Centro Nacional de Biotecnología (CNB)-CSIC, Madrid, Spain*

Corresponding author:

Pieta K Mattila

Tel: +358 2 333 7935

Fax: +358 2 333 7000

E-mail: pieta.mattila@utu.fi

Keywords: MIM, MTSS1, I-BAR, B cell receptor signaling, BCR, B cell activation, adaptive immune response, metabolism, immune response

Abstract

Efficient generation of antibodies by B cells is one of the prerequisites of protective immunity. B cell activation by cognate antigens via B cell receptors (BCR) or pathogen-associated molecules through pattern-recognition receptors, such as Toll like receptors (TLRs), initiates signaling cascades, which leads to transcriptional and metabolic changes that ultimately transform B cells into antibody producing plasma cells or memory cells. BCR signaling and a number of steps downstream of it rely on coordinated action of cellular membranes and the actin cytoskeleton, tightly controlled by concerted action of multiple actin-regulatory proteins, some of them exclusive to B cells. Here, we dissect the role of Missing-In-Metastasis (MIM), or Metastasis suppressor 1 (MTSS1), a cancer-associated membrane and actin cytoskeleton regulating protein, in B cell-mediated immunity by taking advantage of MIM knockout mouse strain. We show undisturbed B cell development and normal composition of B cell compartments in the periphery. Interestingly, we found that $MIM^{-/-}$ B cells are defected in BCR signaling in response to surface-bound antigens but, on the other hand, show increased metabolic activity after stimulation with LPS or CpG. *In vivo* MIM knockout animals exhibit impaired IgM antibody responses to immunization with T cell-independent antigen. This study provides the first comprehensive characterization of MIM in B cells, demonstrates its regulatory role for B cell-mediated immunity, as well as proposes new functions for MIM in the regulation of receptor signaling and cellular metabolism, processes which may also contribute to the poorly understood function of MIM in cancer.

50

51 # Introduction

52

53 Adaptive immune responses, such as efficient clearing of pathogens while maintaining the homeostasis of
54 the host, depend on fine-tuned balance of various signals. Increasing evidence points towards an important
55 role of the actin cytoskeleton and plasma membrane organization at the cross-roads of various signaling
56 pathways orchestrating lymphocyte action (Mattila et al., 2016). In B cells, the actin cytoskeleton enables
57 changes in cell morphology, required, for instance, during the formation of the immunological synapse
58 (Kuokkanen et al., 2015). Interestingly, actin cytoskeleton and plasma membrane also potently regulate B
59 cell receptor (BCR) signaling (Mattila et al., 2013, 2016; Treanor et al., 2010). A plethora of cytoskeletal
60 regulator proteins enable the multifaceted roles of the actin cytoskeleton in living cells. Lymphocytes
61 generally present very characteristic protein expression patterns and considering the specialized functions of
62 these immune cells, it is not surprising that this also holds true for the regulators of the actin cytoskeleton.
63 One best-known example of such protein is Wiscott-Aldrich syndrome (WAS) protein (WASp), a critical
64 regulator of lymphocyte function and an activator of Arp2/3 actin filament (F-actin) nucleator complex
65 (Bosticardo et al., 2009).

66

67 A highly conserved, cancer-associated protein linked to the regulation of both the actin cytoskeleton and the
68 plasma membrane, Missing in Metastasis (MIM) or Metastasis Suppressor 1 (MTSS1), is highly expressed
69 in spleen and particularly in B cells; and information based on BioGPS portal). MIM belongs to a family of
70 proteins with a characteristic inverse Bin, Amphiphysin, Rvs (I-BAR) domain, or IRSp53 and MIM
71 homology domain (IMD), which binds and deforms cellular membranes (Mattila et al., 2007; Safari and
72 Suetsugu, 2012). It also directly interacts with and regulates actin via its C-terminal WH2 domain (WASp
73 homology 2) (Mattila et al., 2003; Woodings et al., 2003) and indirectly via interactions with other actin
74 regulatory proteins, such as cortactin and Rac1 GTPase (Bompard et al., 2005; Cao et al., 2012; Lin et al.,
75 2005; Mattila et al., 2007). Importantly, MIM has been linked to various cancers, either as a putative tumor
76 metastasis suppressor, or promoter (Machesky and Johnston, 2007). Genetic alterations in *MIM/MTSS1*
77 gene were found in 6% of sequenced cancer samples and, depending on the cancer type, both diminished or
78 increased gene expression profiles are seen (Petrov et al., 2019). Regarding hematopoietic malignancies,
79 MIM is upregulated, for example, in hairy cell and mantle cell lymphomas as well as chronic lymphocytic
80 leukaemia (CLL). In CLL, interestingly, the good prognosis samples exhibit highest levels of MIM while
81 the poor prognosis samples show lower MIM levels in comparison (Petrov et al., 2019). In mice, it has been
82 reported that upon aging MIM knockout animals develop lymphomas resembling diffuse large B cell
83 lymphoma (DLBCL) (Yu et al., 2012). Moreover, a degenerative kidney disease, potentially linked to

84 impaired cell-cell junction formation, as well as a defected dendritic spine formation and neuronal
85 alterations have been reported in MIM knockout mice (Saarikangas et al., 2011, 2015). These findings
86 illustrate the complexity of MIM function, the basis of which remains enigmatic due to the lack of
87 understanding about the molecular mechanisms and pathways where MIM acts. Despite of the reported high
88 expression in B cells and the association hematopoietic malignancies, nothing is known about the role of
89 MIM in activation of adaptive immune responses.
90
91 In this study, we took advantage of a MIM knockout mouse model (MIM$^{-/-}$, MIM-KO) (Saarikangas et al.,
92 2011) to explore the physiological role of MIM in B cell compartment, specifically in early B cell activation
93 and mounting of the antibody responses. While we found no defects in B cell development, MIM-deficiency
94 caused a variety of changes in mature B cells. MIM$^{-/-}$ B cells showed significantly reduced signaling upon
95 stimulation with surface-bound antigens mimicking activation via immunological synapse. T cell-
96 independent IgM responses were reduced in MIM$^{-/-}$ mice, while on the other hand, T cell-dependent
97 immune responses appeared normal. Unlike BCR stimulation, MIM$^{-/-}$ B cells were robustly activated by
98 TLR agonists that, interestingly, also led to increased metabolic activity in cells lacking MIM. Our study
99 highlights the complex role of MIM in different cellular functions and can serve as a stepping stone for
100 unveiling the role of MIM in hematopoietic cancers.
101

102 # Materials and Methods

103 *Antibodies and chemicals*

104 List of antibodies and reagents used in the study can be found in Table I.

105 *Table 1. Key resources/reagents table*

Name	Catalog #	Company	Application
AffiniPure Donkey Anti-Mouse IgM, μ Chain Specific	715-005-020	Jackson ImmunoResearch	Stimulatory antibodiies
AF647 AffiniPure F(ab´)$_2$ Fragment Donkey Anti-mouse IgM	715-606-020	Jackson ImmunoResearch	Stimulatory antibodies
Monobiotinylated Purified Rat anti-mouse Ig κ light chain	559749 or 21343	BD Biosciences or Thermo Fisher Scientific	Stimulatory antibodies
Purified Rat Anti-Mouse IgM - Clone II/41 (RUO)	553435	BD Biosciences	ELISA, capture antibody
AffiniPure Goat Anti-Mouse IgG, Fcγ Fragment Specific	115-005-071	Jackson ImmunoResearch	ELISA, capture antibody
Goat Anti-Mouse IgG1-BIOT	1071-08	SouthernBiotech	ELISA, detection antibody
Goat Anti-Mouse IgG2b-BIOT	1091-08	SouthernBiotech	ELISA, detection antibody
Goat Anti-Mouse IgG2c-BIOT	1078-08	SouthernBiotech	ELISA, detection antibody
Goat Anti-Mouse IgG3, Human/Bovine/Horse SP ads-BIOT	1103-08	SouthernBiotech	ELISA, detection antibody
Goat Anti-Mouse IgG Fc-BIOT	1033-08	SouthernBiotech	ELISA, detection antibody
Biotin Rat Anti-Mouse IgM, Clone R6-60.2 (RUO)	553406	BD Biosciences	ELISA, detection antibody
C57BL/6 Mouse Immunoglobulin Panel	5300-01B	SouthernBiotech	ELISA, standard
Purified Rat Anti-Mouse CD16/CD32	553142	BD Biosciences	Flow cytometry, Fc-block
FITC Rat Anti-Mouse IgG1	553443	BD Biosciences	Flow cytometry, CSR
FITC Rat Anti-Mouse IgG2b	553395	BD Biosciences	Flow cytometry, CSR
FITC Rat Anti-Mouse IgG3	553403	BD Biosciences	Flow cytometry, CSR
AffiniPure Goat anti-Mouse IgG2c, FITC-conjugated	115-095-208	Jackson ImmunoResearch	Flow cytometry, CSR
LPS, Lipopolysaccharides from Escherichia coli	L2887-5MG	Sigma-Aldrich	CSR, Metabolism
CpG ODN 1826	tlrl-1826	Invivogen	Metabolism
CD40L, Recombinant Mouse CD40 Ligand/TNFSF5 (HA-tag)	8230-CL-050	R&D Systems	CSR
IL-4, Recombinant Mouse IL-4	404-ML-010	R&D Systems	CSR, Metabolism
IFNγ, Recombinant Mouse IFN-g	575304	BioLegend	CSR
TGF-β, Recombinant Mouse TGF-beta 1	7666-MB-005	R&D Systems	CSR
BD Horizon™ V450 Rat Anti-Mouse IgM Clone R6-60.2	560575	BD Biosciences	Flow cytometry
AF488 anti-mouse IgD [11-26c.2a]	405718	Biolegend	Flow cytometry
AF700 anti-mouse CD19 [6D5]	115528	Biolegend	Flow cytometry
APC anti-mouse CD19 [6D5]	115512	Biolegend	Flow cytometry
APC/Cy7 anti-mouse/human CD45R/B220 [RA3-6B2]	103224	Biolegend	Flow cytometry
APC anti-mouse CD21/CD35 (CR2/CR1) [7E9]	123412	Biolegend	Flow cytometry
Alexa Fluor® 594 anti-mouse CD23 [B3B4]	101628	Biolegend	Flow cytometry
PE anti-mouse CD93 (AA4.1, early B lineage) [AA4.1]	136503	Biolegend	Flow cytometry
PE anti-mouse CD3e [145-2C11]	100308	Biolegend	Flow cytometry
FITC anti-mouse CD4 [GK1.5]	100406	Biolegend	Flow cytometry
APC anti-mouse CD5 [53-7.3]	100626	Biolegend	Flow cytometry
Tom20 (FL-145)	sc-11415	Santa Cruz Biotechnology	Flow cytometry, metabolism
Goat anti-Rabbit IgG (H+L), AF488	A-11008	Thermo Fisher Scientific	Flow cytometry, metabolism
MTSS1 (P549) Ab	4385S	Cell Signaling Technologies	Immunoblotting
MTSS1 (N747) Ab	4386S	Cell Signaling Technologies	Immunoblotting
Phospho-Zap-70 (Tyr319)/Syk (Tyr352) Ab	2701P	Cell Signaling Technologies	Immunoblotting
Syk (D3Z1E) XP¬ Rabbit mAb	13198S	Cell Signaling Technologies	Immunoblotting
Phospho-Lyn (Tyr507) Ab	2731P	Cell Signaling Technologies	Immunoblotting
Lyn (C13F9) rabbit mAb	2796S	Cell Signaling Technologies	Immunoblotting
Phospho-CD19 (Tyr531) Ab	3571S	Cell Signaling Technologies	Immunoblotting

CD19 Ab	3574S	Cell Signaling Technologies	Immunoblotting
Phospho-PI3 Kinase p85 (Tyr458)/p55 (Tyr199) Ab	4228S	Cell Signaling Technologies	Immunoblotting
Phospho-CD19 (Tyr531) Ab	3571S	Cell Signaling Technologies	Immunoblotting
Phospho-Akt (Ser473) (193H12) Rabbit mAb	4058S	Cell Signaling Technologies	Immunoblotting
Akt1 (C73H10) Rabbit mAb	2938S	Cell Signaling Technologies	Immunoblotting
Phospho-NF-kappa-B p65 (Ser536) (93H1) Rabbit mAb	3033S	Cell Signaling Technologies	Immunoblotting
NF-κB p65 (D14E12) XP® Rabbit mAb	8242S	Cell Signaling Technologies	Immunoblotting
p44/42 MAPK (Erk1/2) Ab	9102S	Cell Signaling Technologies	Immunoblotting
Phospho-p44/42 MAPK (Erk1/2) (Thr202/Tyr204) Ab	9101S	Cell Signaling Technologies	Immunoblotting
Phospho-Btk (Tyr223) (D1D2Z) Rabbit mAb	87457	Cell Signaling Technologies	Immunoblotting
Peroxidase AffiniPure Goat Anti-Rabbit IgG (H+L)	111-035-144	Jackson ImmunoResearch	Immunoblotting
Peroxidase AffiniPure Goat Anti-Mouse IgG, Fcγ Specific Ab	115-035-071	Jackson ImmunoResearch	Immunoblotting
Donkey Anti-Rabbit IgG Ab, IRDye 800CW Conjugated	926-32213	LI-COR Biosciences	Immunoblotting
AF555 Phalloidin	A34055	Thermo Fisher Scientific	Microscopy
AF647 anti-mouse/human CD45R/B220 Ab	103229	BioLegend	Microscopy
Anti-Phosphotyrosine Ab, clone 4G10®	05-321	Merck Miilipore	Microscopy
Goat anti-Mouse IgG2b, AF488 conjugate	A-21141	Thermo Fisher Scientific	Microscopy
CXCL13	250-24-5ug	PeproTech	Microscopy, SLB

Mice

MIM knockout mouse colony was a kind gift from Prof. Pekka Lappalainen and Dr. Pirta Hotulainen from the University of Helsinki and Minerva Foundation Institute for Medical Research (Saarikangas et al., 2011). The strain, in C57Bl/6 background, had no apparent health problems until the age of 8 months when mice were latest sacrificed, however, we observed that from all genotyped animals that were kept alive, 18 pups developed hydrocephaly over the study period. Among them, 17 were knockout, 1 heterozygote, and none wild-type. To generate this strain, Saarikangas et al (Saarikangas et al., 2011) introduced a *Neo*-cassette, containing several stop codons, by homologous recombination into Exon 1 of *MIM*/*Mtss1* gene in 129/Sv ES-cells. Chimeric mice were backcrossed to C57Bl/6J background for several generations and the colony in Turku was established by breedings of heterozygote founder animals. All experiments were done with age- and sex-matched animals and WT littermate controls were used whenever possible.

Immunizations

At the age of 3-4 months, groups of WT and *MIM*$^{-/-}$ females were immunized with NP_{40}-FICOLL (F-1420, Biosearch Technologies) for T-independent (TI) immunization or NP_{31}-KLH (N-5060, Biosearch Technologies) for T-dependent (TD) immunization. Each mouse received 50 µg of antigen in 150 µL of PBS (NP_{40}-FICOLL) or PBS/Alum (77161, Thermo Fisher) adjuvant (2:1 ratio) (NP_{31}-KLH) solution by intraperitoneal injection. Blood (~100 µL) was sampled from lateral saphenous veins on day -1 (preimmunization) and every week after immunization on days +7, +14, +21 and +28 for both FICOLL and KLH cohorts. Secondary immunization of KLH cohort was performed on day +135 (0) and

128 blood was sampled on days +134 (-1), +139 (+4), +143 (+8) and +150 (+15). Coagulated blood was
129 spun at +4°C / 2000 rpm for 10 min and serum was collected and stored at -20°C.
130 All animal experiments were approved by the Ethical Committee for Animal Experimentation in
131 Finland. They were done in adherence with the rules and regulations of the Finnish Act on Animal
132 Experimentation (62/2006) and were performed according to the 3R-principle (animal license numbers:
133 7574/04.10.07/2014, KEK/2014-1407-Mattila, 10727/2018).
134
135 *ELISA*
136 Total and NP-specific antibody levels were measured by ELISA on half-area 96-well plates (Greiner
137 Bio-One, 675061). Wells were coated overnight at +4°C with capture antibodies (2 µg/mL) or NP-
138 conjugated carrier proteins, $NP_{(1-9)}$-BSA or $NP_{(>20)}$-BSA (N-5050L, N-5050H, Biosearch Technologies)
139 at 50 µg/mL in 25 µL PBS. Non-specific binding sites were blocked for 2 hours in 150 µL of blocking
140 buffer (PBS, 1%BSA, 0.05 NaN_3). Appropriate dilutions (see below) of 50 µL serum samples in
141 blocking buffer were added for overnight incubation at +4°C. Biotin-conjugated detection antibodies (2
142 µg/mL) in 50 µL of blocking buffer were added for 1 hour followed by 50 µL ExtrAvidin-Alkaline
143 phosphatase (E2636, Sigma-Aldrich, 1:5000 dilution) in blocking buffer for 1 hour at room temperature
144 (RT). In between all incubation steps, plates were washed with 150 µL washing buffer (PBS, 0.05%
145 Tween-20) either 3 times for the steps before sample addition or 6 times after addition of the mouse sera.
146 The final wash was completed with 2 times wash with 150 µL of water. Finally, 50 µL of Alkaline
147 phosphatase-substrate, SIGMAFAST p-Nitrophenyl phosphate, (N2770, Sigma-Aldrich) solution was
148 added and OD was measured at 405 nm. Serum dilutions were determined experimentally to fall into
149 linear part of the dose-response curve of the absorbance measurements for any given isotype and typical
150 values are as follows: IgM levels (1:3000–1:4000), IgG levels (1:20000–1:80000). Different dilutions of
151 AP-streptavidin were used where necessary. Typical time for AP-substrate incubation before
152 measurement was about 30 min at RT.
153 All ELISA samples were run in duplicates, OD values were averaged and blank background was
154 subtracted. Absolute concentrations of total antibody levels were extrapolated from calibration curves
155 prepared by serial dilution of mouse IgM or subclasses of IgG from C57Bl/6 immunoglobulin panel.
156 Relative NP-specific antibody levels were extrapolated from reference curves prepared by serial dilution
157 of pooled serum, in which the highest dilution step received an arbitrary unit of 0.5.
158
159 *Immunophenotyping*
160 All cells were isolated in B cell isolation buffer (PBS, 2% FCS, 1 mM EDTA). Bone marrow cells were
161 isolated by flushing the buffer through mouse femoral and tibial bones. Splenocytes were isolated by

162 mashing the spleen in small buffer volumes with syringe plunger in 48-well plates. Peritoneal cavity
163 cells were isolated by filling the cavity with ~10 mL buffer volume through puncture and collecting the
164 fluid back. Cell suspensions were filtered through 70 µm nylon cell strainers. As a general flow
165 cytometry protocol all following steps were done in flow cytometry buffer I (PBS, 1% BSA). Fc-block
166 was done with 0.5 µL/70 µL anti-mouse CD16/32 antibodies for 10 min and cells were stained for 30
167 min. Washings were done 3 times in 150 µL of flow cytometry buffer I. All steps were carried out on ice
168 in U-bottom 96-well plates at cell density of 0.25–0.5 × 10^6/well. Before acquisition, cells were
169 resuspended in 130 µL flow cytometry buffer II (PBS, 2.5% FCS). Samples were acquired on BD LSR
170 Fortessa, equipped with four laser lines (405 nm, 488 nm, 561 nm, 640 nm). Compensation matrix was
171 calculated and applied to samples either in BD FACSDiva™ software (BD Biosciences) or in FlowJo
172 (Tree Star, Inc) based on fluorescence of conjugated antibodies using compensation beads (01-1111-41,
173 Thermo Fisher Scientific). FMO (fluorescence minus one) controls were used to assist gating. Data was
174 analyzed with FlowJo software.
175
176 *B cell isolation*
177 Splenic B cells were Isolated with EasySep™ Mouse B Cell Isolation Kit (19854, Stem Cells
178 Technologies) according to manufacturer's instructions and let to recover in RPMI (10% FCS,
179 20 mM HEPES, 50 µM β-mercaptoethanol, 1:200 Pen/Strep 10K/10K) in an incubator at +37°C and 5%
180 CO_2 for 1-2 hours.
181
182 *Class-switch recombination and proliferation*
183 Isolated splenic B cells (~10–20×10^6 cells) were stained first with 5 µL (5mM) Cell Trace Violet
184 (C34557, Thermo Fisher Scientific) in 10 mL of PBS for 10 min at RT and let to recover in complete
185 RPMI (+37°C, 5% CO_2) for 1–2 hours. To induce class-switching, B cells were cultured on 24-well
186 plates at 0.5×10^6/mL density in complete RPMI supplemented with indicated doses of LPS (4 µg/mL),
187 CD40L (150 ng/mL), IL-4 (5 ng/mL), IFN-γ (100 ng/mL) and TGF-β (3 ng/mL) for 3 days. Cells were
188 blocked with anti-mouse anti-CD16/32 and stained for 30 min with antibodies against IgG subclasses.
189 Additionally, cells were stained with 4 µg/mL 7-AAD (ABD-17501, Biomol) for live/dead cell
190 discrimination and samples were acquired on BD LSR II equipped with 3 laser lines (405 nm, 488 nm,
191 640 nm) and analyzed with FlowJo software.
192
193 *B cell receptor signaling and immunoblotting*
194 For analysis of BCR signaling, isolated splenic B cells were starved for 10 min in plain RPMI and
195 0.5 × 10^6 cells in 100 µL of plain RPMI were stimulated in duplicates with anti-mouse IgM µ-chain-

196 specific (anti-IgM) antibodies either in solution or bound to the culture dish surface, for 3, 7 and 15 min.
197 For solution stimulation, 5 μg/mL of anti-IgM was used, in 96-well plates. For surface-bound mode, 48-
198 well plates were coated with 5 μg/mL of anti-IgM antibodies in 120 μL of PBS at +4°C, overnight, and
199 washed 3 times with 500 μL of ice-cold PBS before experiment. After activation, B cells were instantly
200 lysed with 25 μL of 5x SDS lysis buffer (final: 62.5 mM TrisHCl pH ~6.8, 2% SDS, 10% Glycerol,
201 100mM β-mercaptoethanol, bromphenol blue) and sonicated for 7.5 min (1.5 mL tubes, high power, 30 s
202 on/off cycle, Bioruptor plus, Diagenode). Lysates (20–30 μL) were run on 8–10% polyacrylamide gels
203 and transferred to PVDF membranes (Trans-Blot Turbo Transfer System, Bio-Rad). Membranes were
204 blocked with 5% BSA in TBS (TBS, pH ~7.4) for 1 hour and incubated with primary antibodies
205 (~1:1000) in 5% BSA in TBST (TBS, 0.05% Tween-20) at +4°C, overnight. Secondary antibody
206 incubations (1:20000) were done for 2 hours at RT in 5% milk in TBST for HRP-conjugated antibodies
207 and with addition of 0.01% SDS for fluorescently-conjugated antibodies. Washing steps were done in 10
208 mL of TBST for 5 × 5 min. Membranes were scanned with Odyssey CLx (LI-COR) or visualized with
209 Immobilon Western Chemiluminescent HRP Substrate (WBKLS0500, Millipore) and ChemiDoc MP
210 Imaging System (Bio-Rad). Phospho-antibodies were stripped in 25 mM Glycine-HCl buffer, pH ~2.5
211 for 10 min, membranes were blocked and probed again for evaluation of total protein levels. Images
212 were background subtracted and the raw integrated densities for each band were measured in ImageJ.
213 Ratios of phosphorylated-vs-total protein levels were analyzed with ratio paired t test. For data
214 presentation these ratios were normalized to WT value at 0 min.
215
216 *Intracellular Ca^{2+} flux*
217 Splenic B cells were resuspended at a concentration of 2.5×10^6 cell/mL in RPMI supplemented
218 with 20 mM HEPES and 2.5% FCS and loaded with 1 μM Fluo-4 (F14201, Thermo Fisher Scientific)
219 and 5 μM Fura Red (F3021, Thermo Fisher Scientific) for 45 min (+37°C, 5% CO_2). Cell suspension
220 was then diluted in 10 volumes of complete RPMI and incubated for 10 min at RT. Cells were
221 centrifuged at 200 g, at RT for 5 min and resuspended at 2.5×10^6 cells/mL in PBS (20 mM HEPES,
222 5 mM glucose, 0.025% BSA, 1 mM $CaCl_2$, 0.25 mM sulfinpyrazone (S9509, Sigma-Aldrich), 2.5%
223 FCS). Anti-mouse IgM antibodies were added into prewarmed (+37°C) B cell suspension aliquots to
224 final concentrations of 5 or 10 μg/mL and cells were acquired on BD LSR Fortessa. Fluorescence of
225 Fluo-4 and Fura Red were recorded by a continuous flow for 5 min. Data was analyzed in FlowJo and
226 presented as ratiometric measurement of Fluo-4/Fura Red median intensity levels.
227 Peritoneal cavity B cells were washed in L-15 medium, resuspended in 75 μL acquisition buffer
228 (HBS (HEPES buffered saline):L-15 (1:1 ratio), 2.5 μM probenecid (P8761, Sigma-Aldrich)) and
229 labeled by addition of 75 μL acquisition buffer with 10 μM Fluo-4 for 5 min at +37°C. Cells were

230 washed in 1 ml, resuspended in 200 µL and divided into two wells. B cells were prestained for 10 min
231 on ice with anti-CD23-AF594 antibodies, washed and resuspended in 100 µL of acquisition buffer on
232 ice. Samples were prewarmed (+37°C) in a total volume of 300 µL of acquisition buffer and 50 µL of
233 anti-IgM $F(ab)_2$-AF633 were added. Cells were acquired on BD LSR Fortessa for 3-5 min and analyzed
234 in FlowJo.
235
236 *Scanning electron microscopy*
237 For the analysis of resting B cells, wells of the microscopy slides (10028210, Thermo Fisher Scientific)
238 were coated with CellTak (354240, Corning) in PBS (3.5 µg/cm^2 of surface area, according to
239 manufacturer's recommendations) for 20 min (RT), washed once with water and allowed to dry. For the
240 analysis of activated B cells, wells were coated with 5 µg/mL of anti-mouse IgM, µ-chain-specific
241 antibodies in PBS for 1 h (RT) and washed in PBS. 10^5 B cells in 20 µL of complete RPMI were placed
242 on coated wells for 10 min (+37°C, 5% CO_2) and fixed by adding 20 µL PFA in PBS (4% PFA final, pH
243 7.0–7.5) for 15 min. Samples were further fixed in 4% PFA/2.5% gluteraldehyde in PBS for 30 min,
244 washed in PBS and post-fixed in 1% OsO_4 containing 1.5% potassium ferrocyanide, and dehydrated
245 with a series of increasing ethanol concentrations (30%, 50%, 70%, 80%, 90%, 96% and twice 100%).
246 Specimens were immersed in hexamethyldisilazane and left to dry by solvent evaporation. The cells
247 were coated with carbon using Emscope TB 500 Temcarb carbon evaporator and imaged with Leo 1530
248 Gemini scanning electron microscope.
249
250 *Microscopy / Cell spreading*
251 MatTek microscopy dishes were coated with 7.5 µg/mL anti-mouse IgM, µ-chain-specific antibodies in
252 PBS at +37°C for 30 min and washed once with PBS. Isolated splenic B cells (10^6) were left unstained
253 or labeled with 0.17 µL of anti-B220-AF647 antibodies in 400 µL PBS for 10 min in 1.5 mL tubes on
254 ice, spun (2500 rpm, 5 min), washed twice in 900 µL of ice-cold PBS and resuspended in 200 µL of
255 Imaging buffer (PBS, 10% FBS, 5.5 mM D-glucose, 0.5 mM $CaCl_2$, 0.2 mM $MgCl_2$). Equal amounts of
256 unstained and labeled cells of different genotypes were mixed and loaded onto coated MatTek dishes at
257 35 µL/well. Cells were incubated for 10 min (+37°C, 5% CO_2), fixed in pre-warmed (+37°C) 4%
258 formaldehyde/PBS for 10 min (RT), permeabilized in 0.1% Triton X-100/PBS for 5 min (RT), washed
259 once with PBS and blocked in blocking buffer (PBS, 1% BSA) at +4°C (overnight). Cells were stained
260 with 1:50 Phalloidin-AF555 and 1:500 anti-pTyr primary antibody (4G10) in blocking buffer for 1 hr
261 (RT), washed 4 times with PBS, and stained with 1:500 secondary anti-mouse IgG2b-AF488 in blocking
262 buffer for 1 hr (RT), washed 4 times in PBS and imaged in PBS with total internal reflection
263 fluorescence (TIRF) mode in DeltaVision OMX Imaging System (GE Healthcare). TIRF images of

264 cortical actin and pTyr were processed with ImageJ macro using B220 and bright-field channels to
265 discriminate between attached WT or MIM-KO cells. Spreading area (determined on pTyr channel),
266 mean fluorescence intensity and total fluorescence intensity (integrated density) of phalloidin and pTyr
267 staining of each cell were analyzed (~50–340 cells per sample). Geometric means of spreading area and
268 fluorescence intensity levels from each experiment were analyzed with paired ratio t test. For cumulative
269 scatter plots, equal numbers (here 92 cells) were randomly selected from each experiment and analyzed
270 with unpaired t test. 3-4 independent experiments were performed for the analysis.
271
272 *Supported lipid bilayers*
273 Artificial planar lipid bilayers containing GPI-linked mouse ICAM-1 (200 molecules/μm^2) were formed
274 as previously described (Carrasco et al., 2004; Grakoui et al., 1999). Briefly, unlabeled GPI-linked
275 ICAM-1 liposomes and liposomes containing biotinylated lipids were mixed with 1,2-dioleoyl-PC
276 (DOPC) (850375P, Avanti lipids, Inc) at various ratios to obtain specified molecular densities. Planar
277 membranes were assembled on FCS2 dosed chambers (Bioptechs) and blocked with PBS/2% FCS for
278 1 h at RT. Antigen was tethered by incubating membranes with AF647-sreptavidin, followed by
279 monobiotinylated anti-kappa light chain antibodies (20 molecules/μm^2). The isolated B from WT and
280 $MIM^{-/-}$ mice cells were labeled with 1μM CFSE (21888, Sigma-Aldrich) or left unlabeled, mixed at 1:1
281 ratio, and injected into prewarmed chambers (4×10^6, +37°C) with 100 nM recombinant murine
282 CXCL13. Confocal fluorescence, differential interference contrast (DIC), and interference reflection
283 microscopy (IRM) images were acquired in different locations at the plane of the cell contact at 15 min
284 after cell injection. All assays were performed in PBS, supplemented with 0.5% FCS, 0.5 g/L D-glucose,
285 2 mM MgCl and 0.5 mM $CaCl_2$. Images were acquired on Zeiss Axiovert LSM 510-META inverted
286 microscope, equipped with 40x oil-immersion objective (Madrid), or Zeiss LSM 780 inverted
287 microscope, equipped with 40x water-immersion objective (Turku), and analyzed by ImageJ and Imaris
288 7.0 (Bitplane). Geometric means of spreading area (determined on IRM channel), area of collected
289 antigen and mean fluorescence intensity of antigen from each experiment (~40–500 cells per
290 experiment) were analyzed with ratio paired t test.
291
292 *Intracellular Ca^{2+} flux on supported lipid bilayers*
293 Splenic WT or $MIM^{-/-}$ B cells (3.2×10^6) were resuspended in 75 μL of L-15 medium and labeled by
294 addition of 75 μL of HBS (HEPES buffered saline), supplemented with 2.5 μM probenecid and 20 μM
295 Fluo4 for 5 minutes at +37°C. Cells were washed in 1 mL HBS-probenecid and resuspended in 500 μL
296 HBS-probenecid for immediate injection into FCS2 chambers. Acquired movies were preprocessed with
297 ImageJ and analyzed with a MATLAB implemented high-throughput software *CalQuo*[2] (Lee et al.,

298 2017). Cells were categorized as single peak, oscillatory or not triggering. Cells showing more than two
299 intensity peaks are classified as oscillatory. Data presented as mean percentages of 3 independent
300 experiments with at least 1000 cells analyzed per experiment.
301
302
303 *Metabolic assay*
304 Splenic B cells were seeded at a density of 10^6 cells/mL in complete RPMI and treated with IL-4
305 (10 ng/mL), anti-mouse IgM (10 μg/mL) + IL-4, LPS (4 μg/mL), or CpG (10 μg/mL) for 24 h in an
306 incubator. Cells were then spun and resuspended in Seahorse XF RPMI (103576-100, Agilent),
307 supplemented with 1 mM pyruvate, 2 mM L-glutamine and 10 mM D-glucose. Cell number was
308 adjusted and $0.15x10^6$ cells were seeded per well on a 96-well XF plate, pre-coated with CellTak
309 (354240, Corning). Plate coating was done with 22.4 μg/mL CellTak in $NaHCO_3$, pH 8.0 at +4°C
310 overnight, followed by two washings with water. Seeded cells were spun at 200 g for 1 min with no
311 break and left for 1 h at 37°C to attach to coated wells in a humidified incubator without CO_2 to avoid
312 medium acidification. Seahorse XF96 plate (101085-004, Agilent) was used following the
313 manufacturer's instructions for XF Cell Mito Stress Test Kit (103015-100, Agilent). In this test,
314 sequentially, 1 μM oligomycin, 2 μM FCCP and 0.5 μM rotenone / antimycin A were added to the
315 media. Oxygen consumption rate (OCR) and extracellular acidification rate (ECAR) data were recorded
316 by WAVE software (Agilent). OCR and ECAR data were normalized to cell count and first baseline
317 measurement of WT cells. Basal, maximum and spare respiratory capacities were extracted with area
318 under curve analysis in GraphPad Prism.
319
320 *Analysis of mitochondria*
321 For TMRE staining, B cells were washed in 150 μL PBS, stained with 1:500 Zombie Violet for
322 dead cell discrimination in PBS on ice, washed 2 × 100μL with complete RPMI and stained with
323 5 nM TMRE (T669, Thermo Fisher Scientific) in 200 μL complete RPMI at RT for 20 min.
324 Resuspended in 150 μL of complete RPMI, cells were immediately analyzed by flow cytometry, on BD
325 LSR Fortessa.
326 For Tom20 staining, B cells were stained with Zombie Violet as described above, fixed with 1.6%
327 formaldehyde in PBS for 10 min, washed 2 × 150 μL PBS, permeabilized with 0.5% Triton X-100 in
328 PBS for 5 min at RT, blocked for 1 h at RT. Incubation with primary Tom20 antibodies was done at
329 1:500 dilution for 30 min, followed by 3 × 150 μL washes, staining with 1:1000 dilution of anti-rabbit-
330 AF488 secondary antibodies, and 3 × 150 μL washes. Cells were then resuspended in 130 μL and
331 analyzed by flow cytometry, on BD LSR Fortessa. Antibody incubations, blocking and washings were

done in flow cytometry buffer I on ice. Geometric mean fluorescence intensities were extracted with FlowJo software. All statistical analyses for metabolic data were done with ratio paired t test.

Statistics

Student's t test was applied to the data comparing WT and MIM-KO groups. B cell development, percentages of cell subsets in the periphery, and immunization data were analyzed with unpaired two-tailed t test. In other experiments, ratio paired t test was applied, where pairing of WT and MIM-KO data was based on the day of the experiment (i.e. same experimental conditions for the cells taken from the pair of WT and MIM-KO mice on that day). For large datasets in microscopy, geometric means were extracted for each biological replicate and means were analyzed as described above. Multiple measures two-way ANOVA was additionally used to compare the antibody responses upon immunization. Data presented as Mean ± SEM, unless stated otherwise. Significance is denoted as * $p<0.05$, ** $p< 0.01$, *** $p< 0.001$, **** $p<0.0001$.

347 ## Results

348 ***Largely normal B cell development and maturation of B cells in MIM$^{-/-}$ mice***

349 Mice with targeted disruption of *Mtss1* gene (MIM$^{-/-}$), lacking the expression of MIM, were generated
350 previously (Saarikangas et al., 2011). Splenic B cells, that normally show robust MIM staining in
351 immunoblot, isolated from these mice showed no detectable MIM expression (Fig. 1A). To investigate
352 the possible functions of MIM in the B cell compartment, we first examined the B cells in the bone
353 marrow. We found no apparent differences in the numbers of CD19^{+} and CD19^{+} IgM^{+} populations
354 between age-matched wild type (WT) and MIM$^{-/-}$ mice (Fig. 1C). We then carried out more detailed
355 analysis of the bone marrow B cells with additional surface markers to resolve consecutive
356 developmental stages from common lymphoid progenitors to immature B cells (gating strategy shown in
357 Suppl. Fig. S1A). We found no significant differences between WT and MIM$^{-/-}$ mice in any of these
358 developmental stages (Fig. 1D).

359

360 Next, we went on to analyze the maturation of B cells and their different subsets in the periphery (gating
361 strategy shown in Suppl. Fig. S2A, B). No defects were observed in the overall percentages of CD19^{+} B
362 cells or major T cell subsets in the spleen (Fig. 1E). Similarly, the proportions of transitional (T1–3),
363 follicular (Fo), and marginal zone (MZ) B cells were not significantly altered, although the MZ B cell
364 compartment appeared slightly elevated (Fig. 1F). A special self-renewing population of B cells
365 concentrate in the peritoneal and pleural cavities. To analyze these B1 cells, we isolated cells from the
366 peritoneal cavity of MIM$^{-/-}$ and WT mice. We found no significant differences in the proportions of
367 CD5^{+} (B1a), CD5^{-} (B1b) or mature peritoneal B cells (B2) (Fig. 1G). These results demonstrate that the
368 development of different B cell subsets, both in the bone marrow as well as in the periphery, does not
369 depend on MIM.

370

371 ***MIM$^{-/-}$ B cells are defected in BCR signaling upon activation with surface-bound antigens***

372 Previous cell biological studies in other cell types, supported by various biochemical assays, have
373 proposed a role for MIM at the interface of the plasma membrane and the actin cytoskeleton (Lee et al.,
374 2007; Lin et al., 2005; Mattila et al., 2003, 2007; Saarikangas et al., 2011, 2015). The actin cytoskeleton
375 is intimately involved in the activation of B cells on antigen presenting cells by enabling the spreading
376 of the cells and the formation of the immunological synapse (Harwood and Batista, 2010). Interestingly,
377 the organization of the plasma membrane and the actin cytoskeleton have also been shown to regulate
378 the signaling capacity of the BCR (Mattila et al., 2013, 2016; Treanor et al., 2010). To examine the role
379 of MIM in BCR signaling, we, first, analyzed the mobilization of intracellular calcium, one of the most
380 dramatic immediate consequences of BCR triggering. We isolated splenic B cells from WT and MIM$^{-/-}$

381 mice, loaded them with Fluo-4 and Fura Red, and stimulated with surrogate antigen, antibodies against
382 IgM BCR (anti-IgM), while analyzing the response by flow cytometry. Ratiometric analysis of Fluo-
383 4/Fura Red fluorescence intensities revealed similar elevation of intracellular Ca^{2+} levels in both WT
384 and $MIM^{-/-}$ B cells (Fig. 2A). We also analyzed the calcium response in peritoneal cavity B cells, which
385 were loaded with Fluo-4, prestained with CD23-Alexa Fluor (AF)-594 just before acquisition and
386 stimulated with AF633-labeled anti-IgM antibodies, allowing distinction between B1 (IgM^+ $CD23^-$) and
387 B2 (IgM^+ $CD23^+$) cells. Intracellular Ca^{2+} mobilization was found comparable between WT and $MIM^{-/-}$
388 cells also in these two B cell subsets (Suppl. Fig. S2C).
389
390 To study the BCR signaling in more detail, we next analyzed activation of individual components of
391 BCR signaling pathway by looking at phosphorylation levels of downstream effector molecules. Splenic
392 B cells were stimulated with soluble or surface-bound anti-IgM antibodies for 3, 7 and 15 min and
393 analyzed by immunoblotting. As expected, both stimulatory conditions induced rapid activation of BCR
394 signaling components, as detected by the levels of phosphorylated signaling proteins. Importantly,
395 $MIM^{-/-}$ B cells showed clear defects in signaling in response to surface-bound anti-IgM. Most of the
396 analyzed molecules, including Syk, CD19, Btk, p65 NF-κB and MAPK1/2 showed significant reduction
397 in their activation (Fig 2B, C). In addition, phospho-PI3K showed a trend of reduction with a p-value of
398 0.0557 at 15 min, whereas a p-value of 0.05 was considered as statistically significant. The signaling
399 components studied can be classified into different cascades from the proximal players to downstream
400 effectors. While $MIM^{-/-}$ cells showed robust defects in proximal signaling molecules, the extent to which
401 they affected the downstream cascades alternated. The defects in PI3K pathway were largely recovered
402 at the level of Akt. At the same time, the levels of pp65 NF-κB and pMAPK1/2 were decreased,
403 suggesting that $MIM^{-/-}$ B cells were inefficient in triggering the diacylglycerol (DAG)-PKC module,
404 targets of which both NF-κB and MAPK1/2 are (Mérida et al., 2010). Interestingly, when we studied
405 activation of BCR by soluble ligand, anti-IgM surrogate antibodies in solution, $MIM^{-/-}$ B cells only
406 showed significant defects in the activation of the proximal kinase Syk, but normal activation of other
407 signaling components (Suppl. Fig S2D). These results place MIM as a regulator of, specifically, BCR
408 signaling by surface-bound antigen, function that clearly depends on the fine-tuned activities of the actin
409 cytoskeleton (Bolger-Munro et al., 2019) and could fit well with the previously postulated role of MIM
410 as an organizer of the actin cytoskeleton-membrane interface.
411
412 ***The morphology and formation of the immunological synapse is unaltered in $MIM^{-/-}$ B cells***
413 The actin cytoskeleton is one of the major organizers of cell shape. To explore whether $MIM^{-/-}$ B cells
414 showed any changes in the overall morphology, we visualized them using scanning electron microscopy

415 (SEM), either in resting state or after 10 min activation by surface-tethered anti-IgM, mimicking the
416 formation of the immunological synapse. In SEM, the morphology of MIM$^{-/-}$ B cells appeared grossly
417 similar to WT cells (Fig. 3A). However, to perform another, more quantitative analysis of cell shape, we
418 turned into fluorescent microscopy. We activated B cells on anti-IgM-coated coverslips and analyzed the
419 area of spreading using total internal reflection fluorescence (TIRF) microscopy, an imaging method
420 ideal for visualization of the cell membrane-coverslip interface. The analysis of the TIRF images
421 revealed that MIM$^{-/-}$ B cells spread slightly but consistently less than their WT counterparts (Fig. 3B).
422 To measure overall phosphorylation at the contact region, we stained the cells with anti-phospho-
423 Tyrosine (pTyr) antibodies. Mean fluorescence intensities of pTyr were also reduced in MIM$^{-/-}$ B cells.
424 The diminished area of spreading and pTyr signaling detected by microscopy are well in line with our
425 results from immunoblotting that also showed impaired BCR signaling. However, based on the SEM
426 data and F-actin staining of the splenocytes, MIM$^{-/-}$ cells do not exhibit major morphological defects in
427 their actin cytoskeleton (Fig. 3B).
428
429 Recognition of surface-bound antigens *in vivo* can involve interaction of B cells with antigenic
430 determinants on substrates of various physical properties. While stiff substrates can include bacterial cell
431 wall components or extracellular matrix-linked antigens, perhaps more typical encounter occurs on the
432 surface of antigen presenting cells, where antigens remain laterally mobile. To understand if MIM$^{-/-}$ B
433 cells can initiate robust BCR signaling upon encounter with mobile antigens, we first settled Fluo-4-
434 loaded WT and MIM$^{-/-}$ B cells on supported lipid bilayers (SLB), containing AF647-labeled anti-kappa
435 antibodies and ICAM-1. Mobilization of Ca^{2+} was imaged for 5 min by spinning disk confocal
436 microscopy and analyzed with the *CalQuo*[2] software package for MATLAB (Lee et al., 2017). Analysis
437 of median Fluo-4 intensity and proportions of MIM$^{-/-}$ B cells with single peak or oscillatory Ca^{2+}
438 intensity profiles revealed no differences between MIM-KO and WT cells (Fig. 3C). Furthermore,
439 during contraction phase of the IS formation, MIM$^{-/-}$ B cells accumulated similar amounts of anti-kappa
440 surrogate antigen in the center of the IS as WT B cells at 10 min timepoint (Fig. 3D). Thus, while MIM
441 modulates BCR signaling and spreading responses upon antigen contact on stiff substrates, upon
442 engagement of membrane-bound mobile antigens the cells are able to engage and gather normal
443 amounts on antigen to the center of the immunological synapse. On membranous surfaces, spreading
444 and contraction response is complemented with fluctuations of F-actin-rich protrusions, making the
445 regulation of the cytoskeletal structures distinct from spreading on stiffer surfaces.
446
447 ***MIM is required for an efficient antibody response against T-independent antigen***

448 To test if the defected signaling in MIM$^{-/-}$ B cells leads into problems in mounting of the immune
449 responses, we went on to examine antibody levels of our mice first at the basal state and then upon
450 immunization with T cell-independent (TI) or T cell-dependent (TD) model antigens. We saw no
451 significant changes in the basal antibody levels in the sera of WT and MIM$^{-/-}$ mice although IgG1,
452 particularly, appeared slightly diminished ($p = 0.076$) (Fig. 4A). To study the development of antibody
453 responses towards TI antigens, we immunized mice with NP-FICOLL (Fig. 4B–D). Throughout the
454 examination time course of 28 days, we found reduced levels of both total and NP-specific IgM in
455 MIM$^{-/-}$ mice (Fig. 4C). Interestingly, we also detected impaired responses in the total levels of IgG
456 subtypes, most profound in IgG2b, while the production of NP-specific IgG subclasses was not impaired
457 (Fig. 4D).
458
459 For immunizations with TD protein antigen, we used NP-KLH in alum and followed up the primary
460 response for four weeks. Four months later, we stimulated a memory response and followed that for 2
461 weeks (Suppl. Fig. S3A). In contrast to TI immunization scheme, we found that MIM$^{-/-}$ mice were as
462 efficient in mounting antibody responses to a protein antigen as their WT counterparts (Suppl. Fig. S3B,
463 C). Analysis of the memory responses also showed equal levels of NP-specific IgG for all subclasses
464 (Suppl. Fig. S3D). Furthermore, we analyzed affinity maturation by comparing binding to low and high
465 densities of NP-epitopes in ELISA, and found no significant differences between WT and MIM$^{-/-}$ mice
466 (Suppl. Fig. S3E).
467
468 In the light of defects in BCR signaling and TI immune responses in MIM$^{-/-}$ mice, normal antigen-
469 specific IgG immune responses may point towards compensation by other signals in the system, such as
470 T cell help. To dissect the B cell intrinsic features linked to IgG antibody responses in more detail, we
471 set up an *in vitro* assay for class-switch recombination (CSR). We provoked B cells to change the
472 isotype of the produced Ig molecules, by mimicking cellular events of pathogen encounter or T cell help
473 during maturation of IgG antibody responses. As expected, 3 days of B cells activation with LPS or
474 CD40L in combination with cytokines induced switching of surface-expressed Ig molecules to different
475 IgG isotypes, as detected by flow cytometry. Consistent with the *in vivo* data on generation of NP-
476 specific IgG antibody responses, MIM$^{-/-}$ B cells switched normally in all tested conditions, producing
477 similar percentages of IgG^{+} cells, indicating that MIM is not required for CSR in response to TLR
478 ligands or CD40L and cytokines. In fact, switching rates into the most common isotypes were even
479 slightly higher for MIM$^{-/-}$ B cells when stimulated with LPS (Suppl. Fig. S4A–D). We also loaded the
480 cells with Cell Trace Violet dye, which allowed us to analyze fluorescence profiles of dividing splenic B
481 cells in response to these stimuli. We found robust proliferation of MIM$^{-/-}$ B cells when they were

482 activated with LPS, CD40L or anti-IgM + CD40L (Suppl. Fig. S4E). Analysis of the proliferation
483 indices (PI) showed close to equal proliferation of MIM-KO and WT cells in all conditions tested.
484 Moreover, the division indices (DI) of MIM$^{-/-}$ B cells were moderately, but significantly, increased in
485 CD40L + IFNg cultures, reflecting smaller numbers of cells left undivided, further indicating normal or
486 even improved ability of MIM$^{-/-}$ cells to react to conditions similar to T cell help.
487
488 Our immunization studies suggest that MIM plays a role in IgM antibody responses to TI type 2
489 antigens, which haptenated FICOLL represents, however, MIM is dispensable for the development of
490 antibodies against TD protein antigens. The ability to switch the antibody class upon polyclonal
491 activation with LPS, TI type 1 antigen, appeared normal. Although by using a conventional MIM
492 knockout mouse model we cannot rule out the influence of other immune and stromal cells on the
493 immune responses generated in vivo, IgM antibody responses to TI antigens are considered to be largely
494 B cell intrinsic and in case of TI type 2 antigens rely primarily on intact BCR signaling. Thus, the
495 defects in IgM antibody responses are in line with the diminished BCR signaling observed in vitro (Fig.
496 2B, C; Fig 3B).
497
498 ***MIM$^{-/-}$ B cells show higher metabolic profile upon LPS and CpG stimulation***
499 Activation of resting lymphocytes triggers dramatic changes in their metabolism when cells turn from
500 quiescent state into active proliferation and differentiation. Upregulated metabolic activity meets the
501 increased energetic demands but also has an impact on signal propagation and transcription, through
502 abundance of energy sources and actions of key metabolic enzymes and metabolites. Thus, changes in
503 metabolism support realization of B cell immune functions or pathological transformation when such
504 activity is dysregulated (Jellusova, 2018; O'Neill et al., 2016). We employed the Seahorse platform to
505 analyze metabolic reprogramming of B cells upon activation. To this end, splenic B cells from WT and
506 MIM$^{-/-}$ mice were cultured for 24 h with either anti-IgM, or TLR agonists, LPS or CpG. The rates of
507 cellular oxygen consumption (oxygen consumption rate, OCR), an estimate of mitochondrial respiration,
508 and extracellular acidification (extracellular acidification rate, ECAR), an estimate of glycolysis, were
509 measured with a Mito Stress test in the Seahorse device. In this assay, serial injections of oligomycin,
510 Carbonyl cyanide-4-(trifluoromethoxy)phenylhydrazone (FCCP) and rotenone/antimycin A (Rot/AA)
511 mixture, sequentially inhibit ATP production, collapse the proton gradient membrane potential and
512 finally shut down mitochondrial respiration. This system allows measurement of the basal OCR,
513 maximal and spare respiratory capacities, as well as determination of non-mitochondrial respiration.
514 We activated WT and MIM$^{-/-}$ B cells with LPS, CpG and IgM + IL-4 for 24 h or kept them largely
515 resting with IL-4 alone (Fig. 5A–D). Notably, we saw a significant increase in the metabolic profile of

516 MIM$^{-/-}$ cells as compared to WT counterparts upon activation with TLR ligands, LPS or CpG (Fig. 5C,
517 D). We observed approximately 30% increase in the basal metabolic activity as well as in the maximal
518 respiratory capacity. The spare respiratory capacity showed over two-fold increase in MIM$^{-/-}$ cells upon
519 LPS activation, while in CpG activated samples the high variability of the spare respiratory capacity
520 impeded concluding on the possible difference. In contrast to TLR stimulations, 24 h activation via BCR
521 led to no difference between WT and MIM$^{-/-}$ cells, neither at the basal or maximum respiration levels
522 (Fig. 5B). Similarly, the levels of glycolytic metabolism, reflected by ECAR values obtained from the
523 same assay, showed elevated levels of glycolysis in MIM$^{-/-}$ B cells when stimulated with TLR ligands
524 but not IgM + IL-4 (data not shown). While the preferred route of ATP generation, reflected by OCR to
525 ECAR ratio, remained relatively constant in different conditions, we observed a shift towards oxidative
526 metabolism in basal metabolic activity of MIM$^{-/-}$ B cells stimulated with CpG (Fig. 5D).
527 Finally, we asked if the higher metabolic activity of MIM$^{-/-}$ B cells reflects a *bona fide* change in
528 the mitochondrial activity or is a result of elevated mitochondrial biogenesis upon TLR-mediated
529 metabolic reprograming. To this end, we stained mitochondria with antibodies against TMRE and
530 Tom20 to assess mitochondrial membrane potential and mitochondrial mass, respectively. In freshly
531 isolated splenic MIM$^{-/-}$ B cells, we found slightly but significantly elevated mitochondrial mass without
532 significant increase in mitochondrial membrane potential (Fig. 5E). After TLR-activation however, WT
533 and MIM$^{-/-}$ B cells showed comparable levels of both mitochondrial membrane potential as well as
534 mitochondrial content (Fig. 5F).
535 Thus, after activation with LPS or CpG TLR ligands MIM$^{-/-}$ B cells show higher metabolic activity
536 that does not result from increased mitochondrial biogenesis. Although we found that these differences
537 diminished after 3 days *in vitro* (data not shown), the results show that MIM affects metabolism of B
538 cells, that may in turn influence, for instance, cell proliferation and differentiation during immune
539 responses. The regulation of metabolic changes as well as the mechanisms of how metabolism affects
540 cell differentiation still remain largely enigmatic. Whether MIM affects B cell metabolism in our assay
541 via regulating TLR ligand signaling, indirectly via regulation of BCR function, or via a separate, novel
542 function regulating the metabolic pathways more directly, remains to be addressed by future studies.
543
544
545

546 **DISCUSSION**

547

548 In this study, we examined the role of the enigmatic, cancer-associated cytoskeleton-membrane linker
549 protein MIM in B cells using a MIM knockout mouse model. MIM is strongly expressed in B cells and
550 previous studies have linked it to B cell lymphomas (Yu et al., 2012). In our mouse model, we found
551 non-disturbed B cell development and basal antibody titers. However, the MIM$^{-/-}$ mice showed
552 diminished TI antibody responses as well as defected BCR signaling, indicating a role in B cell
553 activation and mounting of humoral immune responses. At the same time, MIM$^{-/-}$ B cells showed normal
554 proliferative responses and upregulated metabolic boost upon TLR activation, suggestive of complex
555 regulatory effects in different signaling pathways and cell fitness.

556

557 Predisposition of another MIM knockout mouse strain to lymphomagenesis, reported by Zhan and
558 colleagues, is intriguing (Yu et al., 2012). We found the spleens of MIM$^{-/-}$ mice at the age of 2-7 months
559 normal in size and cellularity, but as we did not perform aging experiments, we cannot preclude
560 problems later in life. Regarding B cell development, confusingly, in the first studies with their MIM$^{-/-}$
561 strain, in 2012, Zhan and colleagues reported aberrant levels of total CD19^{+} or CD19^{+}IgM^{+} cells in the
562 lymphoid organs (Yu et al., 2012). Yet, in their later study, the same group reported normal B cell
563 numbers (Zhan et al., 2016). In our MIM$^{-/-}$ strain, numbers of pre-B cells appeared normal, also when a
564 gating strategy identical to Zhan and colleagues was applied (Suppl. Fig. S2B, C). We postulate that the
565 observed discrepancies may arise from the differences in strain maintenance or from different age of
566 mice at the time of immunophenotyping. The possible consequences of the deletion of MIM for B cell
567 development might also be too subtle to manifest in all models. The mouse strain generated by Zhan and
568 colleagues used embryonic stem (ES) cells with insertion of gene trap sequence between exons 3 and 4
569 (clone CSC156, BayGenomics) (Yu et al., 2011). Notably, an independent attempt to recapitulate the
570 generation of MIM$^{-/-}$ strain with the same clone of ES cells resulted in inefficient use of delivered
571 splicing acceptor (SA) site and considerable expression of full-length Mtss1 mRNA as well as protein
572 expression (Fahrenkamp et al., 2017). However, variation in the remaining expression levels between
573 the animals, reported by Fahrenkamp et al., 2017, seemed notable, indicating lability of the splicing.
574 Lack of MIM expression in analyzed cells was, however, shown by Zhan and colleagues (Yu et al.,
575 2011, 2012). In our strain, based on the insertion of neomycin cassette with several stop codons in the
576 first exon of *Mtss1* sequence, low levels of alternative splicing generating a transcript has been
577 previously observed. However this transcript translates into a N-terminally truncated protein that has the
578 critical I-BAR domain functionally inhibited, and which also did not lead to detectable protein

579 expression in MIM KO animals (Saarikangas et al., 2011). We confirmed clear and repeatable lack of
580 detectable protein expression in our substrain using two different commercial antibodies (Fig. 1A).
581
582 MIM$^{-/-}$ B cells exhibited consistently diminished phosphorylation of several BCR effector molecules
583 upon stimulation of BCR with surface-bound antigen (. 2B, C). This defect was in line with smaller area
584 of spreading and reduced overall tyrosine phosphorylation detected by microscopy at the site of contact
585 with antigen (Fig. 3B). Although lower amount of engaged antigen due to inefficient actin-dependent
586 spreading response may partially contribute to the signaling defects observed in MIM$^{-/-}$ B cells, defected
587 BCR signaling also leads to diminished spreading, generating a feedback loop. Signaling upon soluble
588 antigen stimulation, on the other hand, was mostly normal showing only slight diminution in the levels
589 of pSyk (Fig. 2A; Suppl. Fig. S2D). This suggests that MIM participates in the ability of B cells to
590 discriminate between different types of antigens by playing a specific role in B cell activation on
591 surfaces. Although the differential responses of B cells to different forms of antigen are nowadays
592 widely accepted (Bolger-Munro et al., 2019; Mattila et al., 2016; Snapper, 2018), to our knowledge there
593 are only few molecules, such as CD19 and CD81 (Depoil et al., 2008; Mattila et al., 2013), that have
594 been reported to specifically regulate stimulation by surface-linked antigens with mechanisms likely
595 separate from structural roles in cell adhesion or spreading. We also found that while stimulation with
596 surface-bound antigen resulted to a certain degree in reduced phosphorylation of all the tested BCR
597 effectors, the defects in proximal BCR signaling, exemplified by reduced pSyk and pCD19, did not
598 propagate evenly downstream. Reduced pCD19 seemed to largely spare PI3K pathway (Otero et al.,
599 2001) as pAkt levels are on par with those of WT (Fig. 2B, C). At the same time, levels of both pNF-κB
600 and pMAPK1/2 were significantly reduced, suggesting defected DAG-PKC signaling module (Coughlin
601 et al., 2005; Mérida et al., 2010; Su et al., 2002). PKC-FAK axis has been implicated in the regulation of
602 force-dependent B cell activation (Shaheen et al., 2017), and could be involved in the specific defects in
603 response to surface-bound antigens that we observed. Regarding the previously reported role in
604 lymphomagenesis (Yu et al., 2012), it is worth noting that BCR signaling is also one of the main
605 survival pathways in different types of lymphoma and dysregulated wiring of BCR signaling could play
606 a role in lymphomagenesis (Young and Staudt, 2013).
607
608 Our experiments on supported lipid bilayers (SLB) showed that MIM$^{-/-}$ B cells are able to form
609 signaling-competent BCR-antigen microclusters and gather normal amounts of antigen in the center of
610 the IS in this model system (Fig. 3D). This suggests that coupling of BCR to actin and microtubule
611 cytoskeleton, required for the cell spreading and antigen gathering, respectively (Liu et al., 2012;
612 Schnyder et al., 2011), is not notably defected in these settings. However, results from SLB, which are

613 laterally fluid, cannot be directly compared with B cell stimulation on immobilized antigens or a
614 situation where the cells need to overcome frictional coupling of antigen-presenting molecules to the
615 membrane skeleton of the APC (Ketchum et al., 2014), similarly to observations in T cells (Dillard et
616 al., 2014; Luxembourg et al., 1998). In addition, SLBs in our experiments were functionalized with
617 ICAM-1, which is known to lower the threshold for B cell activation (Carrasco et al., 2004).
618
619 In immunization studies, we found that MIM$^{-/-}$ mice developed impaired IgM antibody responses to NP-
620 FICOLL. On the other hand, the responses appeared normal in NP-KLH immunization, indicating,
621 again, that the defects are specific to the nature of the encountered antigen. FICOLL polysaccharide
622 haptenated with NP is a typical TI type 2 antigen, to which the response is thought to rely mainly on
623 marginal zone B cells and peritoneal cavity B1b cells (Girkontaite et al.; Guinamard et al., 2000; Haas,
624 2011; Hsu et al., 2006). As MIM$^{-/-}$ mice showed normal proportions of peritoneal and splenic B cell
625 compartments (Fig. 1F, G), disproportions in mature B cells populations are unlikely to be responsible
626 for the reduced anti-NP IgM levels (Fig, 4C). As MIM is expressed in T cells only at very low levels
627 (Yu et al., 2012), and the numbers of CD4^{+} T cells (Fig. 1E), antibody responses to TD antigen NP-KLH
628 (Suppl. Fig. S3), as well as the levels of class-switched IgG antibodies to NP-FICOLL itself, appeared
629 normal (Fig. 4D), we also consider the defects in possible indirect T cell help unlikely. Therefore, we
630 suggest that the impaired NP-FICOLL responses in MIM$^{-/-}$ mice are caused by defected B cell receptor-
631 mediated signaling, induced by surface-associated FICOLL molecules. This would be in line with the
632 prevailing idea that *in vivo* B cells recognize and respond to antigens that are immobilized on the surface
633 of other cells in the secondary lymphoid organs (Carrasco and Batista, 2007). In case of NP-KLH
634 stimulation these defects could be rescued by secondary signals, to which, based on our data, MIM$^{-/-}$
635 cells respond well (Suppl. Fig. S3).
636
637 While naïve, resting B cells have a considerably low metabolic profile, upon activation, they elevate
638 their metabolic rates, typically manifested by an increase in oxygen consumption and glycolysis
639 (Akkaya et al., 2018; Caro-Maldonado et al., 2014; Jellusova, 2018; Price et al., 2018). The mitogenic
640 stimuli IgM, LPS and CpG have been shown to dramatically increase metabolic requirements in B cells
641 and, thus, play a key role in this transition, essential for the immune responses and differentiation into
642 antibody secreting cells (Boothby and Rickert, 2017; Jellusova, 2018). Interestingly, we found that after
643 24 h culture with either LPS or CpG, respective stimulators for TLR4 and TLR9, MIM$^{-/-}$ B cells
644 exhibited ~30% increased metabolic activity as measured by basal oxygen consumption rate as well as
645 by maximum and spare respiratory capacities (Fig. 5C, D). This finding indicates increased metabolic
646 demands or activity in cells lacking MIM. Already at resting state, MIM$^{-/-}$ B cells exhibited slightly

647 increased mitochondrial mass, as detected by Tom20 levels, possibly pointing towards enhanced cellular
648 energetics (Fig. 5E). At the same time, LPS and CpG induced similar levels of increase in mitochondrial
649 mass and membrane potential in both WT and MIM-KO cells (Fig. 5F), indicating that metabolic
650 differences do not simply arise from enhanced mitochondrial biogenesis. We also did not observe
651 differences in metabolism when B cells were treated with anti-IgM + IL-4, suggesting specificity in the
652 role of MIM towards TLR signaling-induced metabolic changes (Fig. 5B). The increased metabolic
653 capacity in $MIM^{-/-}$ cells could also partially compensate the effects of compromised BCR signaling upon
654 *in vivo* B cell activation and differentiation. The exact mechanism of the role of MIM in cellular
655 metabolism remains to be further investigated, but it is tempting to speculate of a possible link between
656 altered cellular metabolism, related to cell fitness, and the role of MIM in several cancers.
657
658
659
660
661

662 **Acknowledgements**

663 We are thankful for Laura Grönfors for technical assistance, Dr Maria Georgiadou and Prof Johanna
664 Ivaska for their help and generosity with Seahorse assays, as well as Dr Diana Toivola and Joel Nyström
665 for their help and generosity regarding the reagents for studying mitochondria. Central Animal
666 Laboratory of University of Turku is acknowledged for good care of the mice. We thank Tero Vahlberg
667 from the Biostatistics unit, University of Turku for his advice on statistical analysis. We thank
668 Laboratory of Electron Microscopy at the Institute of Biomedicine, University of Turku. Microscopy
669 and flow cytometry were performed at the Turku Bioscience Cell Imaging and Cytometry core facility,
670 supported by Turku Bioimaging and Euro-Bioimaging consortiums. We thank the personnel for their
671 generous help and expertise. Biocenter Finland is acknowledged for providing the research
672 infrastructures, particularly for cell imaging and cytometry, and electron microscopy.

673

674

675 # References

676

677 Akkaya, M., Traba, J., Roesler, A.S., Miozzo, P., Akkaya, B., Theall, B.P., Sohn, H., Pena, M., Smelkinson, M., Kabat, J., et
678 al. (2018). Second signals rescue B cells from activation-induced mitochondrial dysfunction and death. Nat. Immunol. *19*,
679 871–884.
680 Bolger-Munro, M., Choi, K., Scurll, J.M., Abraham, L., Chappell, R.S., Sheen, D., Dang-Lawson, M., Wu, X., Priatel, J.J.,
681 Coombs, D., et al. (2019). Arp2/3 complex-driven spatial patterning of the BCR enhances immune synapse formation, BCR
682 signaling and cell activation. Elife *8*.
683 Bompard, G., Sharp, S.J., Freiss, G., and Machesky, L.M. (2005). Involvement of Rac in actin cytoskeleton rearrangements
684 induced by MIM-B. J. Cell Sci. *118*, 5393–5403.
685 Boothby, M., and Rickert, R.C. (2017). Metabolic Regulation of the Immune Humoral Response. Immunity.
686 Bosticardo, M., Marangoni, F., Aiuti, A., Villa, A., and Grazia Roncarolo, M. (2009). Recent advances in understanding the
687 pathophysiology of Wiskott-Aldrich syndrome. Blood *113*, 6288–6295.
688 Cao, M., Zhan, T., Ji, M., and Zhan, X. (2012). Dimerization is necessary for MIM-mediated membrane deformation and
689 endocytosis. Biochem. J. *446*, 469–475.
690 Caro-Maldonado, A., Wang, R., Nichols, A.G., Kuraoka, M., Milasta, S., Sun, L.D., Gavin, A.L., Abel, E.D., Kelsoe, G.,
691 Green, D.R., et al. (2014). Metabolic reprogramming is required for antibody production that is suppressed in anergic but
692 exaggerated in chronically BAFF-exposed B cells. J. Immunol. *192*, 3626–3636.
693 Carrasco, Y.R., and Batista, F.D. (2007). B cells acquire particulate antigen in a macrophage-rich area at the boundary
694 between the follicle and the subcapsular sinus of the lymph node. Immunity *27*, 160–171.
695 Carrasco, Y.R., Fleire, S.J., Cameron, T., Dustin, M.L., and Batista, F.D. (2004). LFA-1/ICAM-1 Interaction Lowers the
696 Threshold of B Cell Activation by Facilitating B Cell Adhesion and Synapse Formation. Immunity *20*, 589–599.
697 Coughlin, J.J., Stang, S.L., Dower, N.A., and Stone, J.C. (2005). RasGRP1 and RasGRP3 Regulate B Cell Proliferation by
698 Facilitating B Cell Receptor-Ras Signaling. J. Immunol. *175*, 7179 LP – 7184.
699 Depoil, D., Fleire, S., Treanor, B.L., Weber, M., Harwood, N.E., Marchbank, K.L., Tybulewicz, V.L.J., and Batista, F.D.
700 (2008). CD19 is essential for B cell activation by promoting B cell receptor-antigen microcluster formation in response to
701 membrane-bound ligand. Nat. Immunol. *9*, 63–72.
702 Dillard, P., Varma, R., Sengupta, K., and Limozin, L. (2014). Ligand-Mediated Friction Determines Morphodynamics of
703 Spreading T Cells. Biophys. J. *107*, 2629–2638.
704 Fahrenkamp, D., Herrmann, O., Koschmieder, S., Brümmendorf, T.H., and Schemionek, M. (2017). Mtss1(CSC156) mutant
705 mice fail to display efficient Mtss1 protein depletion. Leukemia.
706 Girkontaite, I., Missy, K., Sakk, V., Harenberg, A., Tedford, K., Pötzel, T., Pfeffer, K., and Fischer, K.-D. Lsc is required for
707 marginal zone B cells, regulation of lymphocyte motility and immune responses.
708 Grakoui, A., Bromley, S.K., Sumen, C., Davis, M.M., Shaw, A.S., Allen, P.M., and Dustin, M.L. (1999). The immunological
709 synapse: a molecular machine controlling T cell activation. Science *285*, 221–227.
710 Guinamard, R., Okigaki, M., Schlessinger, J., and Ravetch, J. V. (2000). Absence of marginal zone B cells in Pyk-2–deficient
711 mice defines their role in the humoral response. Nat. Immunol. *1*, 31–36.
712 Haas, K.M. (2011). Programmed Cell Death 1 Suppresses B-1b Cell Expansion and Long-Lived IgG Production in Response
713 to T Cell-Independent Type 2 Antigens. J. Immunol. *187*, 5183–5195.
714 Harwood, N.E., and Batista, F.D. (2010). Early events in B cell activation. Annu. Rev. Immunol. *28*, 185–210.
715 Hsu, M.-C., Toellner, K.-M., Vinuesa, C.G., and Maclennan, I.C.M. (2006). B cell clones that sustain long-term plasmablast
716 growth in T-independent extrafollicular antibody responses. Proc. Natl. Acad. Sci. U. S. A. *103*, 5905–5910.
717 Jellusova, J. (2018). Cross-talk between signal transduction and metabolism in B cells. Immunol. Lett. *201*, 1–13.
718 Ketchum, C., Miller, H., Song, W., and Upadhyaya, A. (2014). Ligand mobility regulates B cell receptor clustering and
719 signaling activation. Biophys. J. *106*, 26–36.
720 Kuokkanen, E., Šuštar, V., and Mattila, P.K. (2015). Molecular control of B cell activation and immunological synapse
721 formation. Traffic *16*, 311–326.
722 Lee, A.M., Colin-York, H., and Fritzsche, M. (2017). CalQuo 2 : Automated Fourier-space, population-level quantification of
723 global intracellular calcium responses. Sci. Rep. *7*, 1–11.
724 Lee, S.H., Kerff, F., Chereau, D., Ferron, F., Klug, A., and Dominguez, R. (2007). Structural basis for the actin-binding
725 function of missing-in-metastasis. Structure *15*, 145–155.

Lin, J., Liu, J., Wang, Y., Zhu, J., Zhou, K., Smith, N., and Zhan, X. (2005). Differential regulation of cortactin and N-WASP-mediated actin polymerization by missing in metastasis (MIM) protein. Oncogene *24*, 2059–2066.
Liu, C., Miller, H., Orlowski, G., Hang, H., Upadhyaya, A., and Song, W. (2012). Actin reorganization is required for the formation of polarized B cell receptor signalosomes in response to both soluble and membrane-associated antigens. J. Immunol. *188*, 3237–3246.
Luxembourg, A.T., Brunmark, A., Kong, Y., Jackson, M.R., Peterson, P.A., Sprent, J., and Cai, Z. (1998). Requirements for Stimulating Naive CD8+ T Cells via Signal 1 Alone. J. Immunol. *161*, 5226 LP – 5235.
Machesky, L.M., and Johnston, S.A. (2007). MIM: a multifunctional scaffold protein. J. Mol. Med. (Berl). *85*, 569–576.
Mattila, P.K., Salminen, M., Yamashiro, T., and Lappalainen, P. (2003). Mouse MIM, a tissue-specific regulator of cytoskeletal dynamics, interacts with ATP-actin monomers through its C-terminal WH2 domain. J. Biol. Chem. *278*, 8452–8459.
Mattila, P.K., Pykäläinen, A., Saarikangas, J., Paavilainen, V.O., Vihinen, H., Jokitalo, E., and Lappalainen, P. (2007). Missing-in-metastasis and IRSp53 deform PI(4,5)P2-rich membranes by an inverse BAR domain-like mechanism. J. Cell Biol. *176*, 953–964.
Mattila, P.K., Feest, C., Depoil, D., Treanor, B., Montaner, B., Otipoby, K.L., Carter, R., Justement, L.B., Bruckbauer, A., and Batista, F.D. (2013). The actin and tetraspanin networks organize receptor nanoclusters to regulate B cell receptor-mediated signaling. Immunity *38*, 461–474.
Mattila, P.K., Batista, F.D., and Treanor, B. (2016). Dynamics of the actin cytoskeleton mediates receptor cross talk: An emerging concept in tuning receptor signaling. J. Cell Biol. *212*.
Mérida, I., Carrasco, S., and Avila-Flores, A. (2010). Diacylglycerol Signaling: The C1 Domain, Generation of DAG, and Termination of Signals. In Protein Kinase C in Cancer Signaling and Therapy, (Totowa, NJ: Humana Press), pp. 55–78.
O'Neill, L.A.J., Kishton, R.J., and Rathmell, J. (2016). A guide to immunometabolism for immunologists. Nat. Rev. Immunol. *16*, 553.
Otero, D.C., Omori, S.A., and Rickert, R.C. (2001). CD19-dependent activation of Akt kinase in B-lymphocytes. J. Biol. Chem.
Petrov, P., Sarapulov, A. V, Eöry, L., Scielzo, C., Scarfò, L., Smith, J., Burt, D.W., and Mattila, P.K. (2019). Computational analysis of the evolutionarily conserved Missing In Metastasis/Metastasis Suppressor 1 gene predicts novel interactions, regulatory regions and transcriptional control. Sci. Rep. *9*, 4155.
Price, M.J., Patterson, D.G., Scharer, C.D., and Boss, J.M. (2018). Progressive Upregulation of Oxidative Metabolism Facilitates Plasmablast Differentiation to a T-Independent Antigen. Cell Rep. *23*, 3152–3159.
Saarikangas, J., Mattila, P.K., Varjosalo, M., Bovellan, M., Hakanen, J., Calzada-Wack, J., Tost, M., Jennen, L., Rathkolb, B., Hans, W., et al. (2011). Missing-in-metastasis MIM/MTSS1 promotes actin assembly at intercellular junctions and is required for integrity of kidney epithelia. J. Cell Sci. *124*, 1245–1255.
Saarikangas, J., Kourdougli, N., Senju, Y., Chazal, G., Segerstråle, M., Minkeviciene, R., Kuurne, J., Mattila, P.K., Garrett, L., Hölter, S.M., et al. (2015). MIM-Induced Membrane Bending Promotes Dendritic Spine Initiation. Dev. Cell.
Safari, F., and Suetsugu, S. (2012). The BAR Domain Superfamily Proteins from Subcellular Structures to Human Diseases. Membranes (Basel). *2*, 91–117.
Schnyder, T., Castello, A., Feest, C., Harwood, N.E., Oellerich, T., Urlaub, H., Engelke, M., Wienands, J., Bruckbauer, A., and Batista, F.D. (2011). B Cell Receptor-Mediated Antigen Gathering Requires Ubiquitin Ligase Cbl and Adaptors Grb2 and Dok-3 to Recruit Dynein to the Signaling Microcluster. Immunity *34*, 905–918.
Shaheen, S., Wan, Z., Li, Z., Chau, A., Li, X., Zhang, S., Liu, Y., Yi, J., Zeng, Y., Wang, J., et al. (2017). Substrate stiffness governs the initiation of B cell activation by the concerted signaling of PKCβ and focal adhesion kinase. Elife *6*.
Snapper, C.M. (2018). Distinct immunologic properties of soluble versus particulate antigens. Front. Immunol. *9*.
Su, T.T., Guo, B., Kawakami, Y., Sommer, K., Chae, K., Humphries, L.A., Kato, R.M., Kang, S., Patrone, L., Wall, R., et al. (2002). PKC-β controls IκB kinase lipid raft recruitment and activation in response to BCR signaling. Nat. Immunol. *3*, 780–786.
Treanor, B., Depoil, D., Gonzalez-Granja, A., Barral, P., Weber, M., Dushek, O., Bruckbauer, A., and Batista, F.D. (2010). The membrane skeleton controls diffusion dynamics and signaling through the B cell receptor. Immunity *32*, 187–199.
Woodings, J.A., Sharp, S.J., and Machesky, L.M. (2003). MIM-B, a putative metastasis suppressor protein, binds to actin and to protein tyrosine phosphatase delta. Biochem. J. *371*, 463–471.
Young, R.M., and Staudt, L.M. (2013). Targeting pathological B cell receptor signalling in lymphoid malignancies. Nat. Rev. Drug Discov. *12*, 229–243.
Yu, D., Zhan, X.H., Niu, S., Mikhailenko, I., Strickland, D.K., Zhu, J., Cao, M., and Zhan, X. (2011). Murine missing in

779 metastasis (MIM) mediates cell polarity and regulates the motility response to growth factors. PLoS One *6*, e20845.
780 Yu, D., Zhan, X.H., Zhao, X.F., Williams, M.S., Carey, G.B., Smith, E., Scott, D., Zhu, J., Guo, Y., Cherukuri, S., et al.
781 (2012). Mice deficient in MIM expression are predisposed to lymphomagenesis. Oncogene *31*, 3561–3568.
782 Zhan, T., Cao, C., Li, L., Gu, N., Civin, C.I., and Zhan, X. (2016). MIM regulates the trafficking of bone marrow cells via
783 modulating surface expression of CXCR4. Leukemia *30*, 1327–1334.
784
785

786

787 **Footnotes**

788

789 **Funding**

790 This work was supported by the Academy of Finland (grant ID: 25700, 296684, 307313, and 327378; to
791 P.K.M.), Sigrid Juselius and Jane and Aatos Erkko foundations (to P.K.M.), Turku doctoral programme
792 in molecular medicine (TuDMM) (to S.H-P. and M.V.). Magnus Ehrnrooth foundation (to A.V.S.). M.F.
793 and L.C. were supported by the Wellcome Trust (212343/Z/18/Z) and EPSRC (EP/S004459/1).

794

795 **Special abbreviations:** MIM, Missing in metastasis; MTSS1, metastasis suppressor 1

796

797 **Correspondence address:**

798 Pieta Mattila
799 Institute of Biomedicine, MediCity Research Laboratories, University of Turku, Finland; and Turku
800 Bioscience, University of Turku and Åbo Akademi University, Turku, Finland
801 Tel: +358 50 574 0780
802 Fax: +358 2 333 7000
803 E-mail: pieta.mattila@utu.fi

804

805 **Competing interests:** No competing interests declared.

806

807 ## Figure legends

808

809 **Figure 1. Normal B cell development and composition of B cell compartments in the bone marrow,**
810 **spleen and peritoneal cavity of MIM$^{-/-}$ mice.**

811 **A.** Equal numbers of WT and MIM-KO splenic B cells were lysed and analyzed by immunoblotting
812 with MTSS1 antibodies (4385S (Ab #1), 4386S (Ab #2), Cell Signaling Technology). Arrowhead
813 indicates the position of the band corresponding to MIM. **B.** Bone marrow, spleen and peritoneal cavity
814 cell populations from WT and MIM$^{-/-}$ mice were extracted for analysis by flow cytometry (C-G) using
815 the gating strategy shown in Supplementary Fig. S1 and S2. Schematic partially created with BioRender
816 software. Data of 3–7 independent experiments is shown as mean ± SEM. **C.** Percentages of total CD19^{+}
817 and CD19^{+} IgM^{+} cells in the bone marrow. **D.** Percentages of B cell precursor and mature B cell
818 populations in the bone marrow. Progression through consecutive B cell developmental stages was
819 analyzed based on the major surface phenotypic markers shown in the schematic below. Percentage of
820 parent populations are shown as mean ± SEM. **E.** Percentages of CD19^{+} B cells and total (upper panel)
821 as well as CD4^{+} and CD8^{+} T cell populations (lower panel) in the spleen. **F.** Percentages of major B cell
822 subsets in the spleen. T1–3 (transitional 1–3), Fo (follicular), MZ (marginal zone) B cells are analyzed.
823 **G.** Percentages of CD23^{-}CD5^{+} (B1a), CD23^{-}CD5^{-} (B1b), CD23^{+}CD5^{-} (B2) B cells in the peritoneal
824 cavity.

825

826 **Figure 2. MIM deficiency leads to impaired B cell receptor signaling in response to surface-bound**
827 **antigen.**

828 **A.** Flow cytometry analysis of Ca^{2+} mobilization in response to BCR stimulation in solution. Splenic B
829 cells from WT or MIM-KO mice were labeled with Fluo-4 and Fura Red and stimulated with 5 or 10
830 µg/mL anti-IgM antibodies. Time of anti-IgM antibody addition is indicated by an arrow. Data is
831 presented as a ratio of Fluo-4 to Fura Red median fluorescence intensity. Representatives of 3
832 independent experiments are shown. **B.** Splenic B cells were stimulated on surfaces coated with
833 5 µg/mL anti-IgM antibodies for 0, 3, 7 and 15 min and lysed. Lysates were subjected for
834 immunoblotting for phosphorylated forms of different BCR signaling effector proteins.
835 Unphosphorylated forms of the corresponding proteins were used as loading control, except for pCD19,
836 pBtk and pPI3K, where NF-κB p65, Syk or Akt were used as loading controls. **C.** Quantification of the
837 data in (B). Data is presented as ratios of phosphorylated forms to total protein levels and normalized to
838 the level of WT at 0 min. Data is from 4-8 independent experiments. Mean ± SEM is shown. * $p<0.05$,
839 ** $p< 0.01$, *** $p< 0.001$.

840

841 **Figure 3. MIM$^{-/-}$ B cells show diminished spreading on antigen-coated glass, but gather normal**
842 **levels of antigen on supported lipid bilayers.**
843 **A.** Scanning electron micrographs of WT and MIM-KO splenic B cells at resting state, let to adhere on
844 CellTak-coated coverslips, or let to spread and get activated on coverslips coated with 5 µg/mL anti-IgM
845 for 10 min. Scale bar, 1 µm. **B.** Splenic B cells were stimulated on coverslips coated with 7.5 µg/mL
846 anti-IgM antibodies for 10 min, fixed, permeabilized and stained with phalloidin (F-actin) and anti-
847 phospho-Tyrosine antibodies (pTyr). Samples were imaged with TIRF microscopy. Representative
848 images showing cell spreading and F-actin staining, are shown (upper left). Area of spreading was
849 analyzed by signal thresholding in pTyr channel (lower left panels), and pTyr (upper right panels) and F-
850 actin (lower right panels) intensities inside cell perimeter were quantified using ImageJ. Mean (MFI) and
851 total (total) fluorescence intensities of pTyr and F-actin stainings are shown, and the mean fluorescence
852 intensity is presented both as pairwise comparison of geometric means of individual experiments (on the
853 left) and as scatter plots of random sampling of 92 cells from each of 3-4 individual experiments
854 (middle). Mean ± SEM is shown. Scale bar, 5 µm. **C.** Intracellular Ca^{2+}-flux was analyzed in splenic
855 WT and MIM-KO B cells loaded with Fluo-4 and stimulated with anti-kappa light chain antibodies
856 tethered on supported lipid bilayers (SLB). A spinning disk confocal microscope was used to record the
857 Fluo-4 intensity and the intracellular Ca^{2+} levels were quantified with *CalQuo*[2] software. Representative
858 images of stimulated B cells, 85 sec after injection into the chamber are shown (upper panel). Mean
859 percentages of non-triggering cells and cells with single peak or oscillatory responses are shown (lower
860 panel). Data of 3 independent experiments. Scale bar, 100 µm. **D.** Splenic WT and MIM-KO B cells
861 were stimulated with AF647–labeled anti-kappa light chain antibodies tethered on SLBs. A laser
862 scanning confocal microscope was used to detect IRM signal (upper left panels) corresponding to the
863 area of contact and to measure the amount of antigen collected after 15 min of activation (lower left
864 panels). The data was quantified for spreading area (IRM Area), antigen (Ag) area and antigen
865 fluorescence intensity (panels on the right). Data is from 3 independent experiments. Mean ± SEM is
866 shown. Scale bar, 1 µm. * $p<0.05$, ** $p< 0.01$, *** $p< 0.001$, **** $p<0.0001$
867
868 **Figure 4. MIM-deficiency results in impaired IgM response and reduced levels of total IgGs**
869 **during T cell-independent immune response.**
870 **A.** Basal antibody levels of major immunoglobulin subclasses were measured from 17–18 WT and
871 MIM KO mice. **B.** A schematic representation of T cell-independent (TI) immunization study. **C.** The
872 antibody responses of immunized WT and MIM-KO mice were followed from serum samples as in (B).
873 Total and NP-specific antibody levels of different immunoglobulin isotypes were measured with ELISA.
874 7-8 mice per group. Mean ± SEM is shown. * $p<0.05$, ** $p< 0.01$.

875

876 **Figure 5. MIM-deficient B cells show increased metabolic activity upon stimulation with Toll-like**
877 **receptor ligands LPS and CpG.**

878 **A–D.** Oxygen consumption rate (OCR) profiles of WT and MIM-KO splenic B cells stimulated with
879 IL-4 (**A**), IgM + IL-4 (**B**), LPS (**C**), or CpG (**D**), for 24 h were measured in a Seahorse XF Cell Mito
880 Stress Test assay. The different steps of the assay are depicted in the graph on the left showing
881 mean ± range. Comparisons of baseline mitochondrial respiration as well as maximum and spare
882 respiratory capacities, extracted from the assay, are shown in the graphs in the middle, and
883 quantification of the ratio of OCR to ECAR (extracellular acidification rate) at the baseline is shown on
884 the right. Data is from 3–4 independent experiments. Mean ± SEM is shown. **E–F.** Splenic B cells,
885 either left unstimulated (E) or stimulated with LPS or CpG for 24 h (F), were loaded with TMRE to
886 extract the mitochondrial membrane potential, or stained with anti-Tom20 antibodies to derive total
887 mitochondrial mass. The samples were analyzed by flow cytometry. Data of 3 independent experiments.
888 Mean ± SEM is shown. * $p<0.05$.

889

890

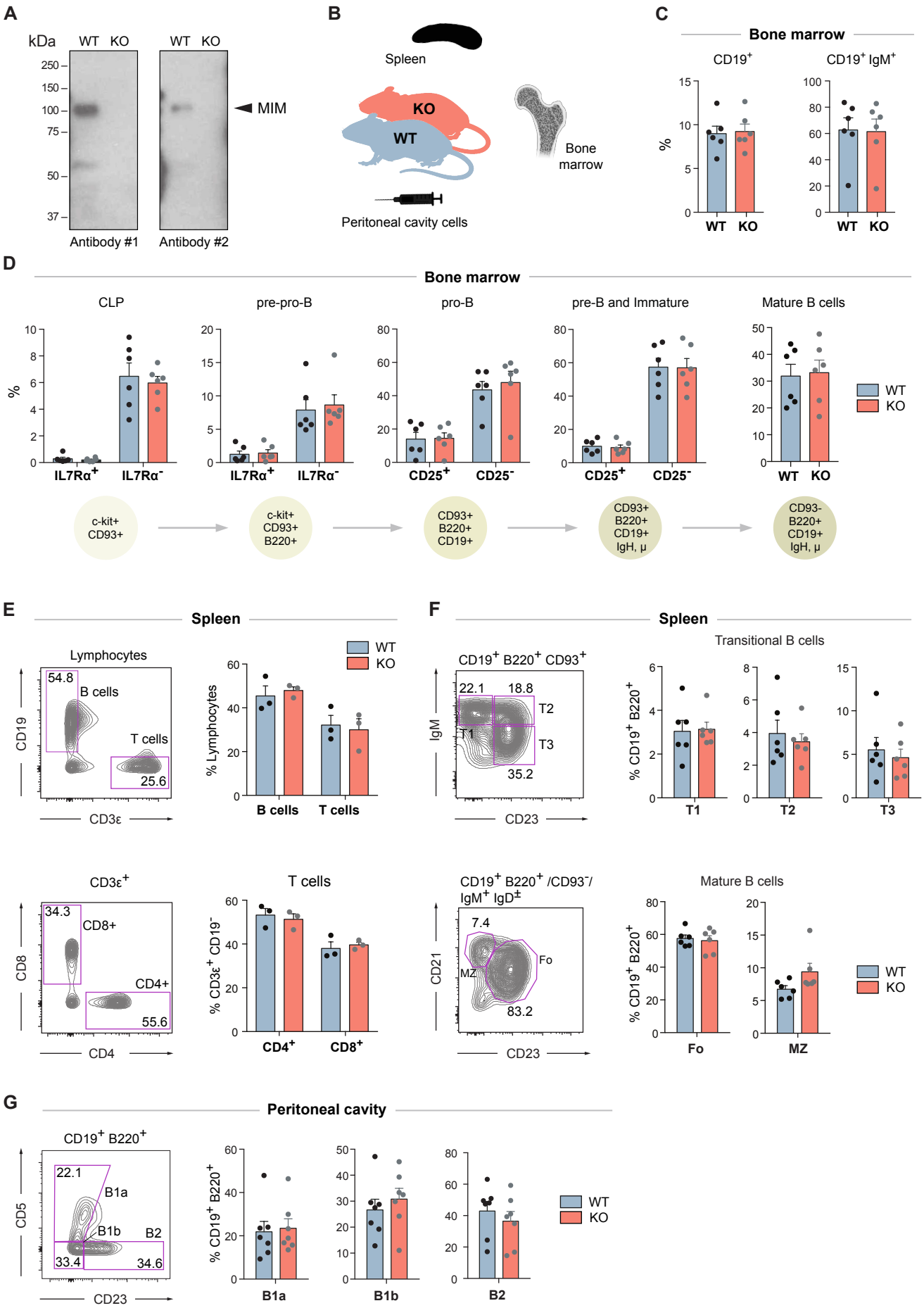
A
kDa
WT KO
WT KO
250
150
100
75
50
37
MIM
Antibody #1
Antibody #2
B
Spleen
KO
WT
Bone marrow
Peritoneal cavity cells
C
Bone marrow
CD19+
CD19+ IgM+
%
WT KO
WT KO
D
Bone marrow
CLP
pre-pro-B
pro-B
pre-B and Immature
Mature B cells
%
IL7Rα+ IL7Rα-
IL7Rα+ IL7Rα-
CD25+ CD25-
CD25+ CD25-
WT KO
WT
KO
c-kit+ CD93+
c-kit+ CD93+ B220+
CD93+ B220+ CD19+
CD93+ B220+ CD19+ IgH, μ
CD93- B220+ CD19+ IgH, μ
E
Spleen
Lymphocytes
54.8
B cells
T cells
25.6
CD19
CD3ε
WT
KO
% Lymphocytes
B cells T cells
CD3ε+
34.3
CD8+
CD4+
55.6
CD8
CD4
T cells
% CD3ε+ CD19-
CD4+ CD8+
F
Spleen
CD19+ B220+ CD93+
22.1
18.8
T2
T1
T3
35.2
IgM
CD23
Transitional B cells
% CD19+ B220+
T1 T2 T3
CD19+ B220+ /CD93-/ IgM+ IgD±
7.4
Fo
MZ
83.2
CD21
CD23
Mature B cells
% CD19+ B220+
Fo MZ
WT
KO
G
Peritoneal cavity
CD19+ B220+
22.1
B1a
B1b
B2
33.4
34.6
CD5
CD23
% CD19+ B220+
B1a B1b B2
WT
KO

Figure 1

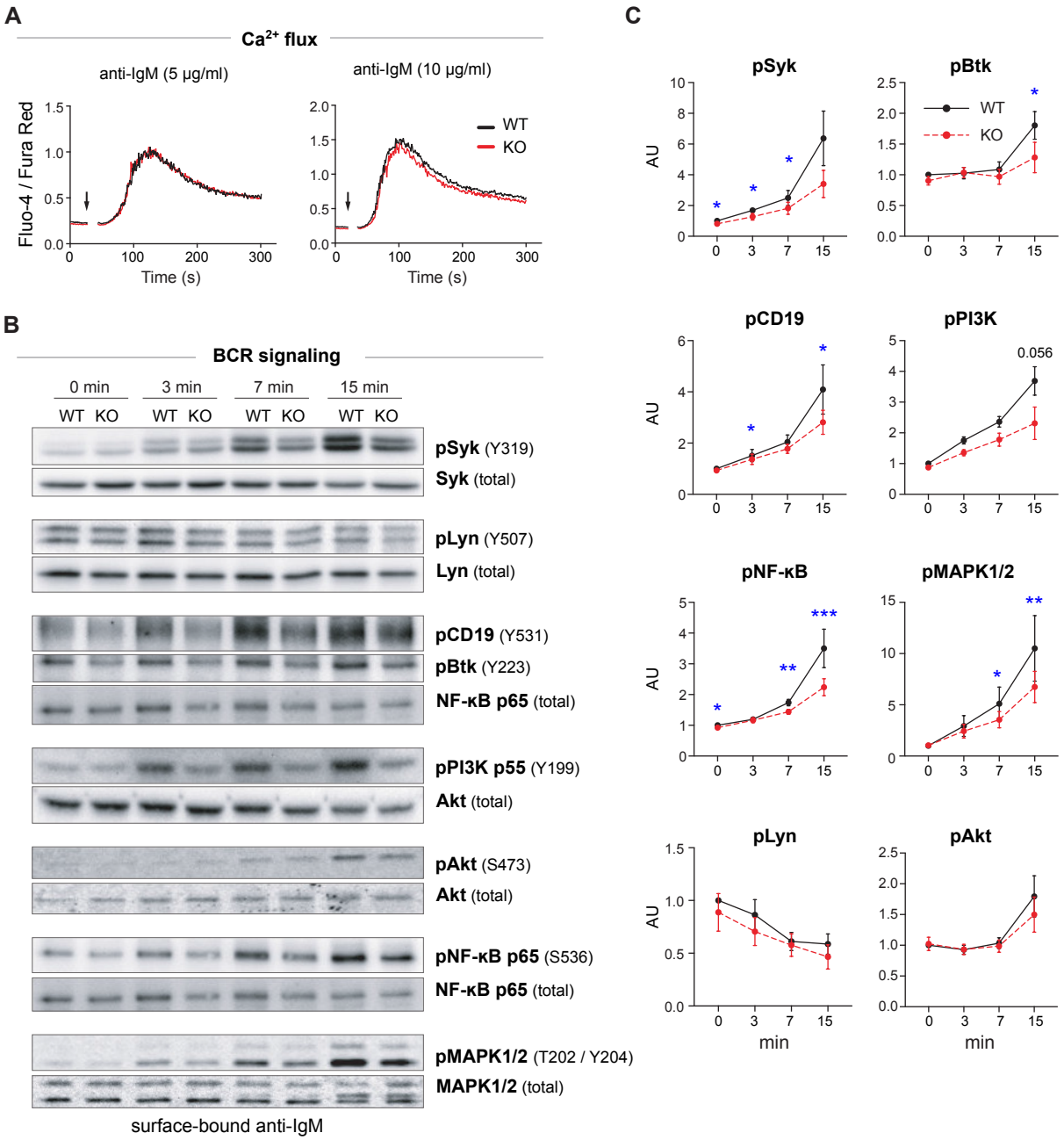
A
Ca2+ flux
anti-IgM (5 µg/ml)
anti-IgM (10 µg/ml)
Fluo-4 / Fura Red
Time (s)
WT
KO
B
BCR signaling
0 min
3 min
7 min
15 min
WT KO WT KO WT KO WT KO
pSyk (Y319)
Syk (total)
pLyn (Y507)
Lyn (total)
pCD19 (Y531)
pBtk (Y223)
NF-κB p65 (total)
pPI3K p55 (Y199)
Akt (total)
pAkt (S473)
Akt (total)
pNF-κB p65 (S536)
NF-κB p65 (total)
pMAPK1/2 (T202 / Y204)
MAPK1/2 (total)
surface-bound anti-IgM
C
pSyk
pBtk
pCD19
pPI3K
pNF-κB
pMAPK1/2
pLyn
pAkt
AU
min
0.056

Figure 2

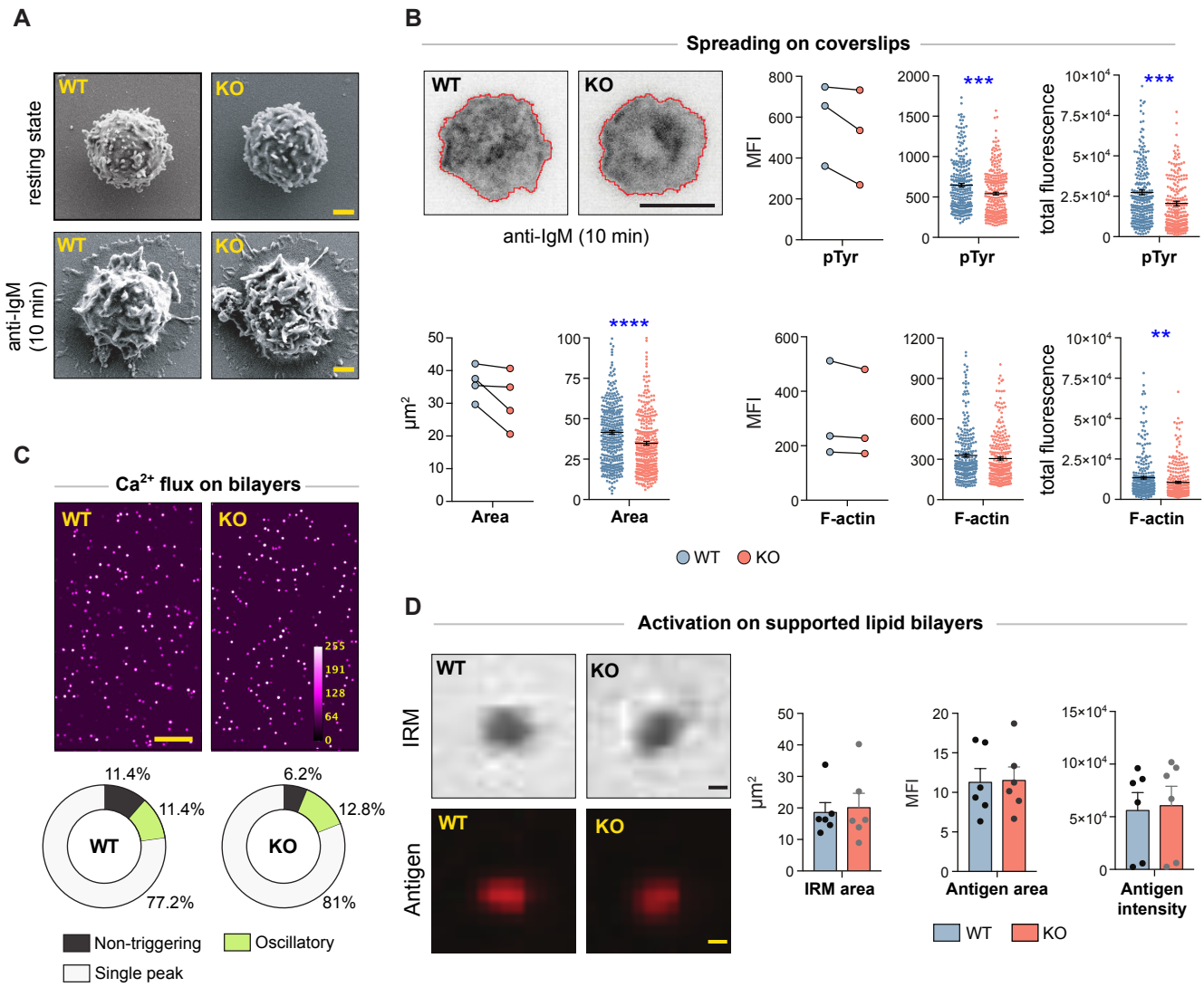
A
resting state
anti-IgM (10 min)
WT
KO
B
Spreading on coverslips
anti-IgM (10 min)
MFI
pTyr
total fluorescence
***
μm²
Area
****
F-actin
**
WT
KO
C
Ca2+ flux on bilayers
255
191
128
64
0
11.4%
11.4%
77.2%
6.2%
12.8%
81%
Non-triggering
Oscillatory
Single peak
D
Activation on supported lipid bilayers
IRM
Antigen
IRM area
Antigen area
Antigen intensity

Figure 3

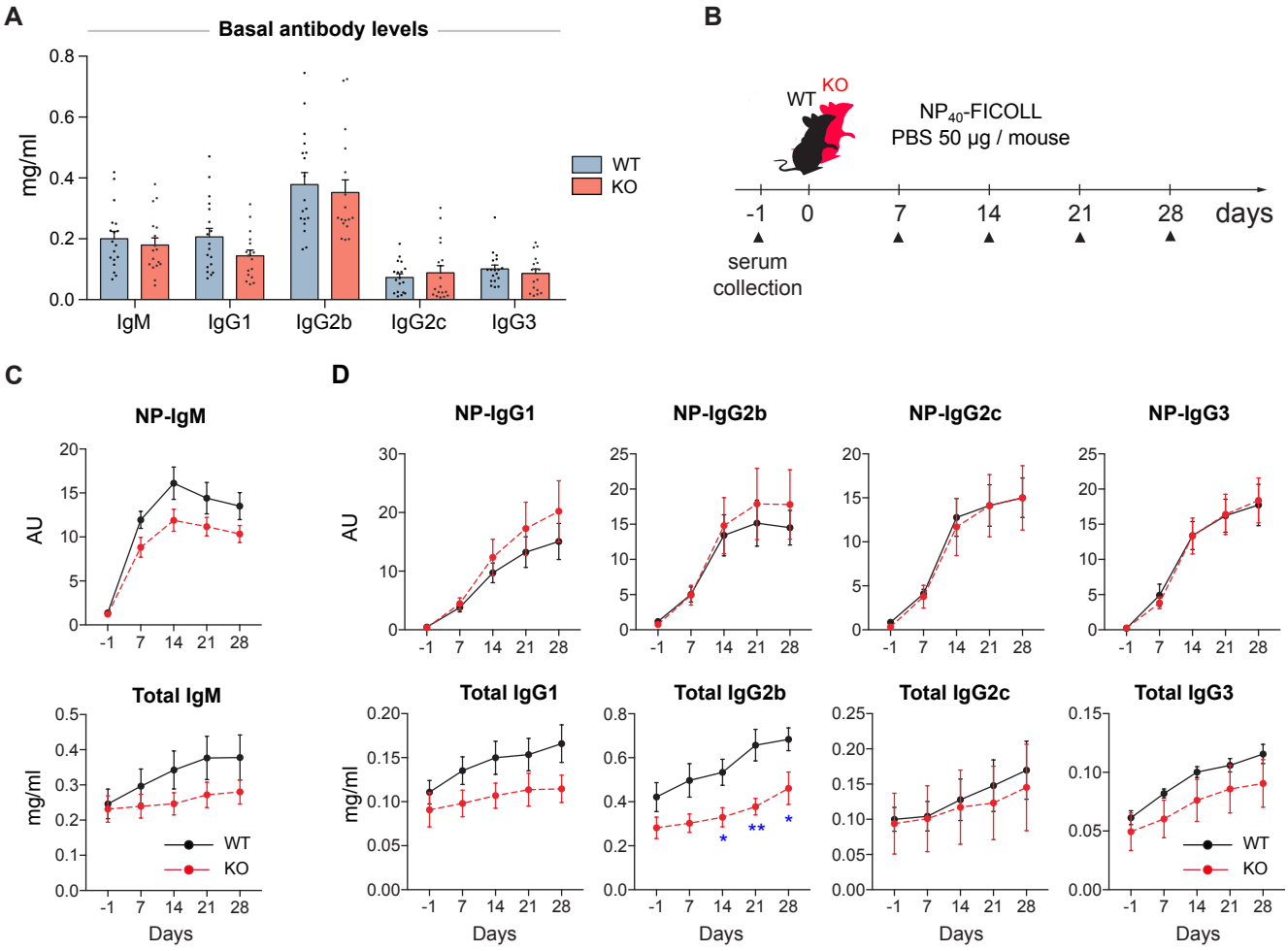
A
Basal antibody levels
mg/ml
0.8
0.6
0.4
0.2
0.0
IgM
IgG1
IgG2b
IgG2c
IgG3
WT
KO
B
WT
KO
NP40-FICOLL
PBS 50 µg / mouse
-1
0
7
14
21
28
days
serum
collection
C
NP-IgM
AU
Total IgM
mg/ml
Days
D
NP-IgG1
NP-IgG2b
NP-IgG2c
NP-IgG3
Total IgG1
Total IgG2b
Total IgG2c
Total IgG3

Figure 4

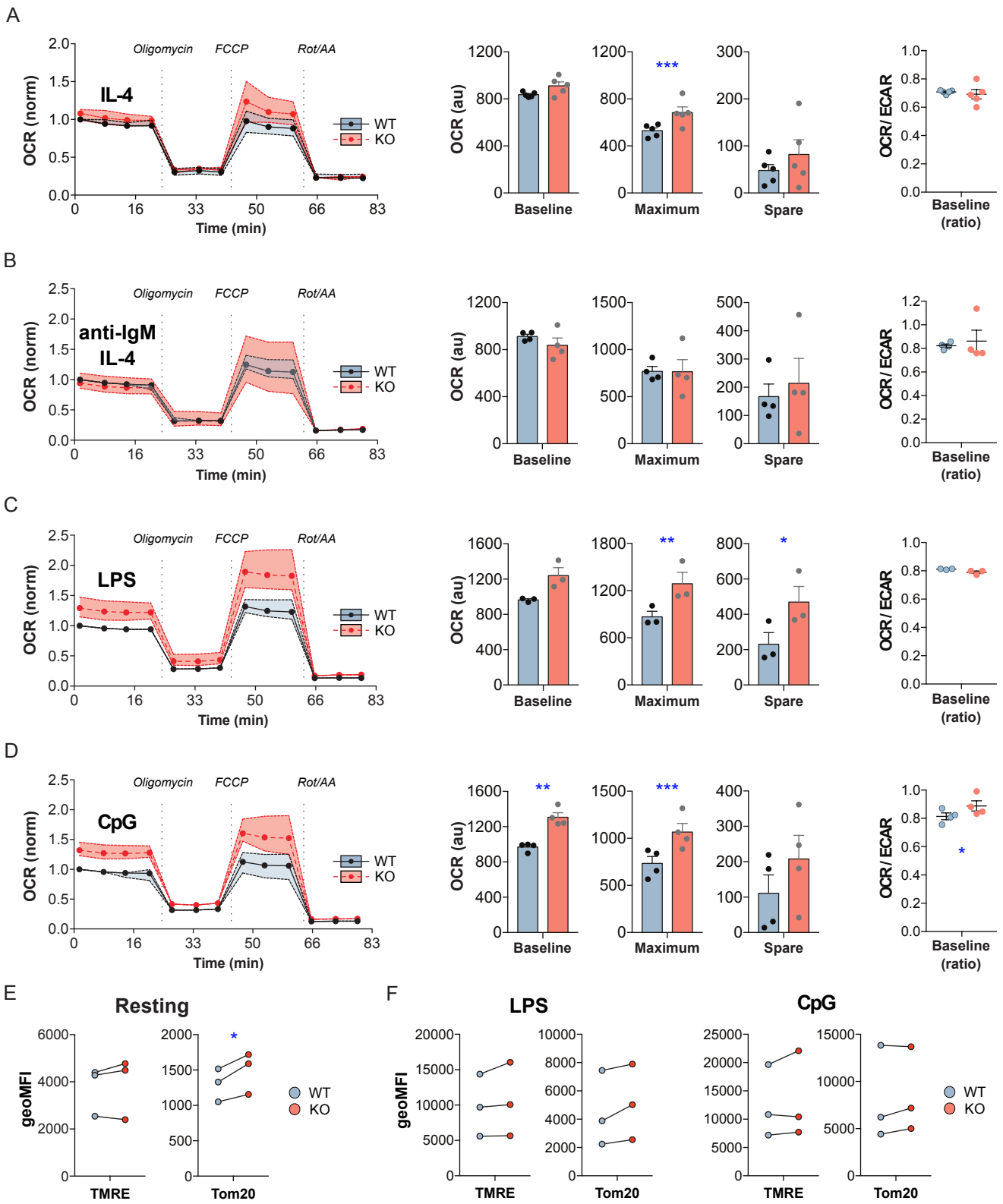
A
IL-4
Oligomycin
FCCP
Rot/AA
OCR (norm)
Time (min)
WT
KO
OCR (au)
Baseline
Maximum
Spare
OCR/ ECAR
Baseline (ratio)
B
anti-IgM
IL-4
C
LPS
D
CpG
E
Resting
geoMFI
TMRE
Tom20
F
LPS
CpG

Figure 5